NAVAL
POSTGRADUATE
SCHOOL

MONTEREY, CALIFORNIA

THESIS

RADIATION DETECTION AND CLASSIFICATION OF HEAVY OXIDE INORGANIC SCINTILLATOR CRYSTALS FOR DETECTION OF FAST NEUTRONS

by

Jacob W. Capps

June 2016

Thesis Advisor:	Craig F. Smith
Co-Advisor:	Fabio Alves

Approved for public release; distribution is unlimited

THIS PAGE INTENTIONALLY LEFT BLANK

REPORT DOCUMENTATION PAGE		*Form Approved OMB No. 0704–0188*
Public reporting burden for this collection of information is estimated to average 1 hour per response, including the time for reviewing instruction, searching existing data sources, gathering and maintaining the data needed, and completing and reviewing the collection of information. Send comments regarding this burden estimate or any other aspect of this collection of information, including suggestions for reducing this burden, to Washington headquarters Services, Directorate for Information Operations and Reports, 1215 Jefferson Davis Highway, Suite 1204, Arlington, VA 22202-4302, and to the Office of Management and Budget, Paperwork Reduction Project (0704-0188) Washington, DC 20503.		
1. AGENCY USE ONLY *(Leave blank)*	**2. REPORT DATE** June 2016	**3. REPORT TYPE AND DATES COVERED** Master's thesis
4. TITLE AND SUBTITLE RADIATION DETECTION AND CLASSIFICATION OF HEAVY OXIDE INORGANIC SCINTILLATOR CRYSTALS FOR DETECTION OF FAST NEUTRONS		**5. FUNDING NUMBERS**
6. AUTHOR(S) Jacob W. Capps		
7. PERFORMING ORGANIZATION NAME(S) AND ADDRESS(ES) Naval Postgraduate School Monterey, CA 93943-5000		**8. PERFORMING ORGANIZATION REPORT NUMBER**
9. SPONSORING /MONITORING AGENCY NAME(S) AND ADDRESS(ES) N/A		**10. SPONSORING / MONITORING AGENCY REPORT NUMBER**
11. SUPPLEMENTARY NOTES The views expressed in this thesis are those of the author and do not reflect the official policy or position of the Department of Defense or the U.S. Government. IRB Protocol number ____N/A____.		
12a. DISTRIBUTION / AVAILABILITY STATEMENT Approved for public release; distribution is unlimited		**12b. DISTRIBUTION CODE**

13. ABSTRACT (maximum 200 words)

Improved detection of fast neutrons can help prevent illicit nuclear materials from being trafficked, and potentially used on American soil. To detect fast neutrons, most current systems use a multi-step process of thermalizing the neutrons, providing a medium or material for neutron capture or other interaction, and then detecting the resultant gamma radiation signal. Heavy inorganic oxide scintillators can detect fast neutrons without thermalization. Simplifying the complex, multi-step detection process into a single interaction and detection medium reduces the detection system's complexity while improving efficiency, compactness, and cost effectiveness.

To understand how such scintillators respond to gamma and neutron radiation, we exposed selected scintillators to different gamma and neutron sources and measured the resulting emission responses with photomultiplier tubes and photonic devices. The resultant emission responses were found to depend on a variety of factors including temperature, crystal fabrication, and structure. In addition to considering these factors, the target material's relationship of response to the effective atomic number, Zeff, was characterized. Follow-on work is recommended to further characterize fast neutrons' spectral response to irradiation.

14. SUBJECT TERMS heavy oxide inorganic scintillators, detection of fast neutrons, spectroscopy, gamma induced scintillation, neutron induced scintillation, spectral response, diffuse source, collimated source			**15. NUMBER OF PAGES** 101
			16. PRICE CODE
17. SECURITY CLASSIFICATION OF REPORT Unclassified	**18. SECURITY CLASSIFICATION OF THIS PAGE** Unclassified	**19. SECURITY CLASSIFICATION OF ABSTRACT** Unclassified	**20. LIMITATION OF ABSTRACT** UU

THIS PAGE INTENTIONALLY LEFT BLANK

RADIATION DETECTION AND CLASSIFICATION OF HEAVY OXIDE INORGANIC SCINTILLATOR CRYSTALS FOR DETECTION OF FAST NEUTRONS

Jacob W. Capps
Major, United States Army
B.S., Tuskegee University, 2003

Submitted in partial fulfillment of the
requirements for the degree of

MASTER OF SCIENCE IN APPLIED PHYSICS

from the

NAVAL POSTGRADUATE SCHOOL
June 2016

Approved by: Craig F. Smith, Ph.D.
Thesis Advisor

Fabio Alves, Ph.D.
Co-Advisor

Kevin B. Smith, Ph.D.
Chair, Department of Physics

THIS PAGE INTENTIONALLY LEFT BLANK

ABSTRACT

Improved detection of fast neutrons can help prevent illicit nuclear materials from being trafficked, and potentially used on American soil. To detect fast neutrons, most current systems use a multi-step process of thermalizing the neutrons, providing a medium or material for neutron capture or other interaction, and then detecting the resultant gamma radiation signal. Heavy inorganic oxide scintillators can detect fast neutrons without thermalization. Simplifying the complex, multi-step detection process into a single interaction and detection medium reduces the detection system's complexity while improving efficiency, compactness, and cost effectiveness.

To understand how such scintillators respond to gamma and neutron radiation, we exposed selected scintillators to different gamma and neutron sources and measured the resulting emission responses with photomultiplier tubes and photonic devices. The resultant emission responses were found to depend on a variety of factors including temperature, crystal fabrication, and structure. In addition to considering these factors, the target material's relationship of response to the effective atomic number, Z_{eff}, was characterized. Follow-on work is recommended to further characterize fast neutrons' spectral response to irradiation.

THIS PAGE INTENTIONALLY LEFT BLANK

TABLE OF CONTENTS

LIST OF FIGURES

LIST OF TABLES

THIS PAGE INTENTIONALLY LEFT BLANK

LIST OF ACRONYMS AND ABBREVIATIONS

A	Atomic mass number
BaF_2	Barium Fluoride
Ba-137	Barium-137
BGO	Bismuth Germenate-20x10
BGO1	Bismuth Germenate-20x30x11
CWO	Cadmium Tungstate
Co-60	Cobalt-60
Cs-137	Cesium-137
Ce^+	Ionized cerium
DOD	Department of Defense
e-h	electron-hole
E_g	bandgap energy
E_γ	incoming energy ray or neutron
e-p	electron-positron
eV	electron volt
GaAs	Galium Arsenide
GaAsP	Galium Arsenide Phosphate
ISC	Institute of Scintillator Crystals
LuAG	Lutetium-aluminum garnate
LGSO	Lutetium-gadolinium orthosilicate
LTCFP	Light tight chamber with femptowatt photoreceiver
MeV	mega-electron volt
Na-22	Sodium-22
Ne-22	Neon-22
Ni-60	Nickel-60
PCS	Photon counting spectrometer
PMT	Photomultiplier Tube
PVC	Polychloride Vinyl
Pu	Plutonium

PWO	Lead Tungstate
SEM	Scanning Electron Microscope
STE	Self-trapped exiton
U	Uranium
USMA	United States Military Academy
USNA	United States Naval Academy
WMD	Weapons of Mass Destruction
Z	Atomic Number
Z_{eff}	Z effective

ACKNOWLEDGMENTS

THIS PAGE INTENTIONALLY LEFT BLANK

I. INTRODUCTION AND BACKGROUND

Protecting the United States from a nuclear attack requires the ability to detect a nuclear weapon before it is used. According to former Secretary of Defense Chuck Hagel, the three pillars of national defense are protecting the homeland, building security globally, and projecting power and winning decisively [1]. Nuclear material detection is embedded in two of these three pillars, yet current detectors for fast neutrons from nuclear weapons materials are bulky, expensive, and have low efficiencies, well below 10% [2]. However, previous research has found that the use of heavy oxide scintillators can overcome these obstacles, in part by leveraging the signal from inelastic scattering of fast neutrons within these scintillators [2], [3]. The purpose of this work is to characterize scintillation response to gamma and neutron radiation in order to contribute to research in this field and to expand upon the basic knowledge of these crystals. Ultimately, the knowledge of their response characteristics will help, in part, create a more efficient and cost-effective detection device that will help the United States and our allies detect and deter nuclear weapon use by any enemy.

A. BACKGROUND

In order to understand the physics of scintillators and how they react, one needs a decent background on nuclear weapons and inelastic scattering, scintillation, and photonics. Understanding these concepts allows one to map the process from the nuclear material's emission of fast neutrons to the measurement of light in a photomultiplier tube (PMT) which completes the nuclear detection string. The fissile fuel of a nuclear weapon, normally U-235 and/or Pu-239, can theoretically be passively detected through the spontaneous fission of constituent isotopes of uranium and plutonium, which produce fast neutrons, and these fast neutrons can be detected with the help of scintillators [4]. Fast neutrons are characterized by energies in excess of 1 MeV (Mega-electron volt) [5]. They can interact with crystalline structures in a variety of ways, but the most important interaction for our application is inelastic scattering. Inelastic scattering is the process in which fast neutrons interact with atomic nuclei in the target material in such way that

1

the kinetic energy of the system is not conserved. In such interactions, the resulting gamma radiation as well as the recoil of the nucleus and further scattering of the re-emitted neutron cause ionizations to occur and electron-hole (e-h) pairs to be created, and these excite the scintillator crystalline structures by e-h pair recombination which ultimately emit photons of visible light that a PMT can count. The nuclear material passive detection process using scintillators is describable in a relatively straightforward way, but the processes involved are relatively complex, which is revealed as the depth of inquiry is increased.

1.   Nuclear Weapon/Spontaneous Fission

Understanding of the basic structure of a nuclear weapons fuel, the spontaneous fission processes that occur in this fuel, and the principles of inelastic scattering and other neutron-matter interactions allows one to understand how detecting fast neutrons is possible using scintillators in which the neutron interactions take place within the detection scintillation crystals. There are three principal types of material that could be used to create a fission nuclear device. In these materials, the process of spontaneous fission (i.e., a fission reaction of an unstable atom without neutron or other initiating interaction) producing fission products and fast neutrons occurs. The resulting spontaneous fission neutrons, when they pass through the scintillator crystal material, can elastically scatter, inelastically scatter, be absorbed, cause other nuclear interactions, or pass through the crystal without interaction. The nuclear interactions that do take place represent the beginning of a process that ultimately result in the scintillator crystal releasing energy in the visible light spectrum for ease of detection.

According to Glasstone and Dolan [4] as well as numerous other experts, there are fundamentally three isotopes that could practically be used to create a fission nuclear bomb—U-235 (Uranium-235), U-233, and Pu-239 (Plutonim-239)—because fission can readily be induced in these isotopes by neutrons of any energy, and because they are stable enough to be stored without appreciable decay [4]. Additionally, the abundant isotopes U-238 and Th-232 (Thorium-232) are capable of neutron-induced fission, but only by neutrons of high energy. These isotopes are considered "fissionable" but not

"fissile," and are therefore not practical materials by themselves to fuel a fission weapon. Nevertheless, residual U-238 is generally present in highly enriched uranium (which is predominantly U-235), and its ability to spontaneously fission, even if at low rates, means that it can produce passive fast neutron emissions. Similarly, isotopes present in weapons grade Plutonium (which is predominantly Pu-239), especially Pu-240, are capable of spontaneous fission and therefore provide a source of fast neutrons. It is important to note that this fast neutron emission will be key to detection of special nuclear material using scintillators.

At the nuclear level, fission is the splitting of a heavy atomic nucleus with the corresponding release of energy, neutrons and fission products; and fusion is the combination of light atomic nuclei, also with an associated release of energy [5]. Fission and fusion are the basic nuclear reactions that produce the destructive power of a nuclear weapon. However, in the context of this thesis, the discussion is focused on the spontaneous fission reaction that is associated with special nuclear weapons material. These materials produce fast neutrons that can be detected with appropriate detection instrumentation. To understand the energy released from the fission process, a further breakdown of "binding energy" is required.

The forces that hold the nucleus of an atom together are reflected and associated as "binding energy." For context, a heavy nucleus of uranium has a binding energy of about 7.5 MeV per nucleon [6]. Fission is the process in which the nucleus of an atom breaks into roughly two equal pieces [5]. This mainly occurs in heavy atoms like uranium and plutonium [5]. The source of the energy released in fission is the breaking of the binding forces holding an atom together. Coupled with the binding energy of an atomic nucleus, there are repulsive forces due to the positive charges of protons present in the nucleus as well. In small atoms, these repulsive forces are overpowered by the "binding energy," which is the reason why smaller atoms do not spontaneously fission. Induced fission is the splitting of an atom due to instability caused by the absorption of a neutron or other outside mass or energy source. Figure 1 shows how a typical neutron-induced fission reaction takes place.
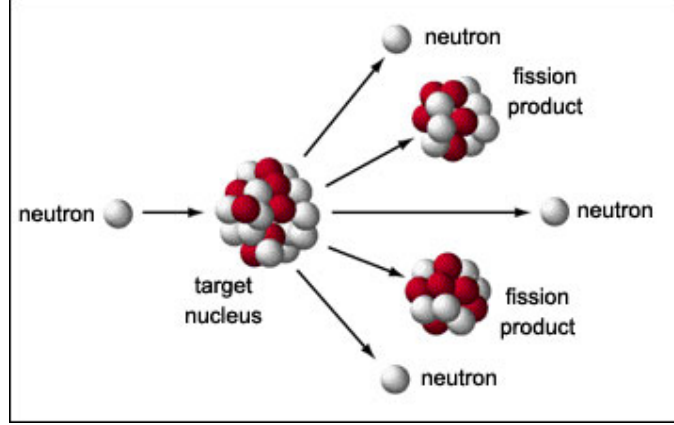
Figure 1.   Induced fission example. Source: [7].

The basic concepts of induced and spontaneous fission are very similar. The primary difference between them is that spontaneous fission depends on the prior instability of the atom, which can be characterized by a semi-empirical mass formula [6]. According to Krane, if Z is the atomic number (number of protons), and A is the number of nucleons (protons plus neutrons), then the formula below characterizes the conditions for this instability [8]:

$$\frac{Z^2}{A} \geq 47 \tag{1}$$

Thus, an atom becomes increasingly unstable relative to the square of the Z number. Although the coefficient 47 is a rough estimate based on empirical observations, it can be used efficiently for heavier atom characterization [6]. After spontaneous fission occurs, one of the bi-products is one or more dislodged neutrons, which can induce fission in neighboring nuclei and react with a scintillator crystal causing elastic or inelastic scattering or other interactions within the detection medium. The target nucleus in the detection medium then reacts by recoiling and directly causing ionizations, or by emitting gamma rays, which also cause ionizations. These processes then create e-h pairs upon interaction with the crystal, which then recombine and emit photons. This is the dominant feature in the scintillation reaction.

2. Gamma-matter Interactions

As shown in Figure 1, once fission occurs—whether induced or spontaneous—several products are produced. Among these are the fast neutrons, that can enter the scintillator crystal and interact with its constituent atoms. These interactions can be of many different types including elastic scattering, inelastic scattering, neutron absorption, or various other neutron-matter interactions. For fast neutrons, inelastic scattering is the preferred type of interaction for our application, especially in interactions with heavy atoms. In such reactions, in addition to kinetic recoil, the emission of gamma radiation as well as a scattered neutron takes place. The resulting gamma radiation can interact with matter in three ways: Compton scattering, the photoelectric effect, or electron-positron pair production [5]. As shown in Figure 2, the probability of which reaction takes place is a function of the gamma energy [9]. However, it is important to note that at energies higher than 1.02 MeV, e-p pair production becomes increasingly important [5].
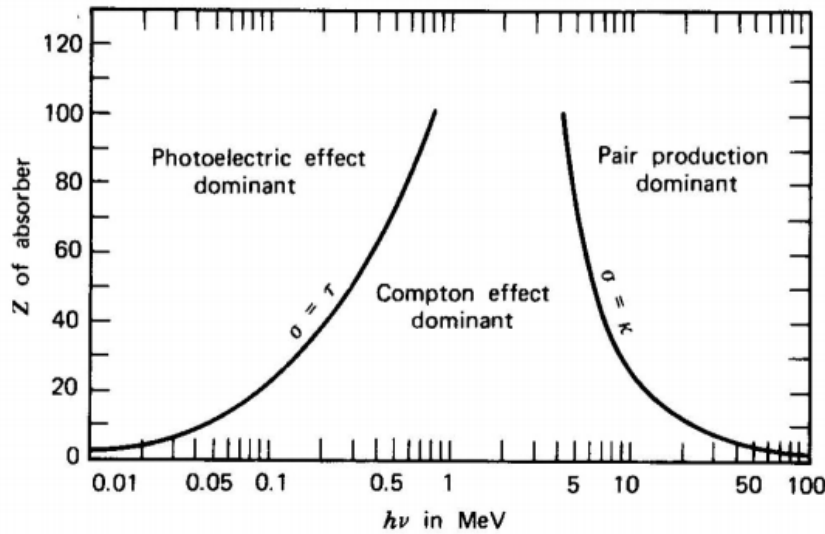
Figure 2.   Regions of gamma interaction dominance. Source:[9].

The photoelectric effect takes place when an incident photon ejects an electron from a material [10]. Compton scattering is where the incoming photon recoils from the target and the target bounces off the incoming particle when at rest [5]. E-p pair production is when the photon is converted to matter – an electron-positron pair. It is important to

recognize that each of these reactions can occur within a scintillator crystal as a result of gamma-matter interactions.

Compton scattering and the photoelectric effect are similar to each other in principle and intuition. In the photoelectric effect, an incoming photon hits an electron; the electron absorbs the energy of the photon and is dislodged from the atom. In Compton scattering, some energy is transferred to the scattered electron and the remaining particle is rejected in another direction [10]. The photoelectric effect will prove to be critical later as this is also the primary means used to count incident photons emitted from a material using a PMT. Figure 3 is a graphic example of the photoelectric effect using a photocathode. As previously stated, as the incoming photon hits the photocathode, an electron is shot from that material and measured with a collector.
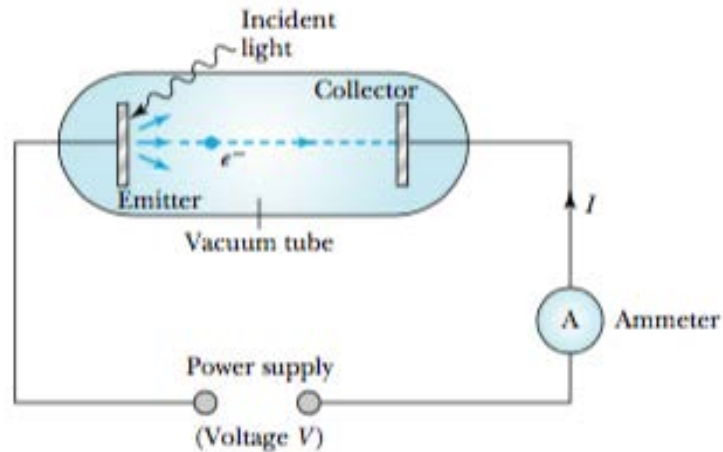
Figure 3.   Photoelectric effect, producing electron. Source: [10].

Comparatively, in Figure 4, both the target and the incoming particle have been displaced by the same occurrence. Compton scattering is prevalent in scintillators below the 1.02 MeV threshold discussed in the e-p pair production section, and the resulting disturbance to the crystal produces scintillation. To illustrate this fact, according to Rodnyi, "the cross section of Compton scattering σ_c decreases with energy E_γ and increases with the number of electrons Z in an atom" [11].

$$\sigma_c \propto \frac{Z}{E_\gamma} \tag{2}$$

One such reaction can lead to another as the scattered photon interacts, and then another which will cause a cascade of ionization until the energy is no longer capable of sustaining that reaction [11].
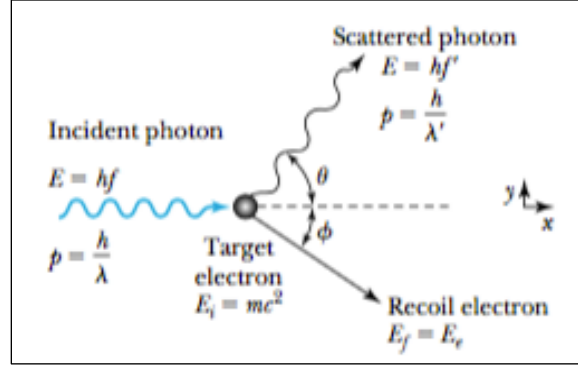
Figure 4.   Compton scattering of a photon by an electron. Source [10].

The third possibility of gamma reaction in a scintillator crystal, after inelastic scattering, is e-p pair production, which occurs in the Coulomb field of the nucleus [11].

For gamma energies above the 1.022 MeV threshold (i.e., double the rest mass value of an electron, 0.511 MeV), there is a growing probability of e-p pair production. E-p pair production is production of a free roaming "e," and a positron "p," which are created by energy levels of this magnitude [5]. The probability of e-p occurrence can be calculated. According to Rodnyi, "The probability of pair production in the nuclear field increases with the nuclear charge and the energy approximately as [11]:

$$\sigma_{pr} \propto Z^2 2 \ln 2 E_\gamma \tag{3}$$

where Z is the atomic number the material and E_γ is the incoming radiation energy in MeV."

3.   Atomic Number (Z)/Density (Z_{eff})

In this study, a comprehensive review was carried out to assess the role of Z in order to understand its impact on light production after fast neutron interaction. According to Figure 5, it would seem likely that as atomic number and matrix density (Z_{eff}) are increased, the probability of neutron interaction within a crystal structure increases. According to Bushuev, the effect of increasing atomic number (Z) on neutron inelastic cross section is gradual but definite [3].
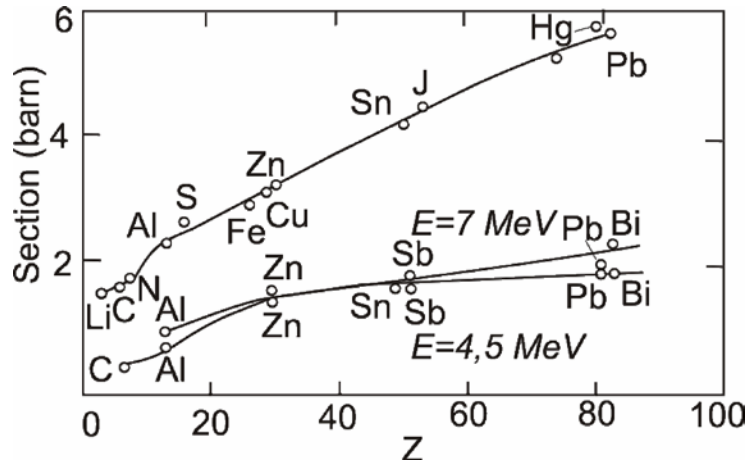
Figure 5.   Inelastic scattering cross section (lower curves) of target nuclei with atomic number (Z) for the neutron energies 4.5 MeV and 7 MeV.
Source: [3].

As shown in Figure 5, as the Z number increases, inelastic scattering cross section increases, while increasing incident energy has a relatively minor effect. This suggests that Z number is more important for the interactions of scintillator crystals and can help us determine interaction probability. Additionally, how tightly the atoms are placed within a crystal combined with the effects of Z should contribute to the understanding of the probability of neutron or gamma interaction. After the nuclei in crystalline material produce a gamma ray from inelastic scattering, the gamma ray subsequently causes ionization in the crystal, and e-h pairs are created.

4.   Scintillation

The process as a whole in which incoming radiation energy is transferred into multiple photons is called scintillation [11]. The basic steps to scintillation that result in light emission are: (1) the neutron-matter interaction (2) subsequent ionization in the material resulting from gammas or recoil of particles (3) the ionization process causing e-h pairs in the material (4) the recombination of e-h pairs results in production of visible light photons. The visible light photons are e-h pair recombinations that occur at the luminescence center [11]. The luminescent center is an activator impurity, and according to Awadalla, "the activator creates special sites in the crystal lattice, creating energy states within the forbidden gap through which an excited electron can de-excite back to the valence band" [12]. The valence band is where electrons are bound at lattice sites, and the conduction band is where electrons are free to migrate throughout the crystal [13]. The luminescence center's band gap is important, Awadalla states, "luminescence centers determine the emission spectrum of the scintillator" [12]. For example, as shown in Figure 6(a), a schematic diagram of the luminescent center, in this case Ce^{3+}, has energy levels of 4f and 5d, and after an electron has been excited to the conduction band, it can de-excite from $D_{5/2}$ to $F_{7/2}$ by emitting a visible photon. For further explanation in Figure 6(b), an exiton (e-h pair traveling to conduction band) will roam freely until it comes in contact with an activator site, and de-excite to the ground configuration ultimately resulting in the creation of scintillation light [12].
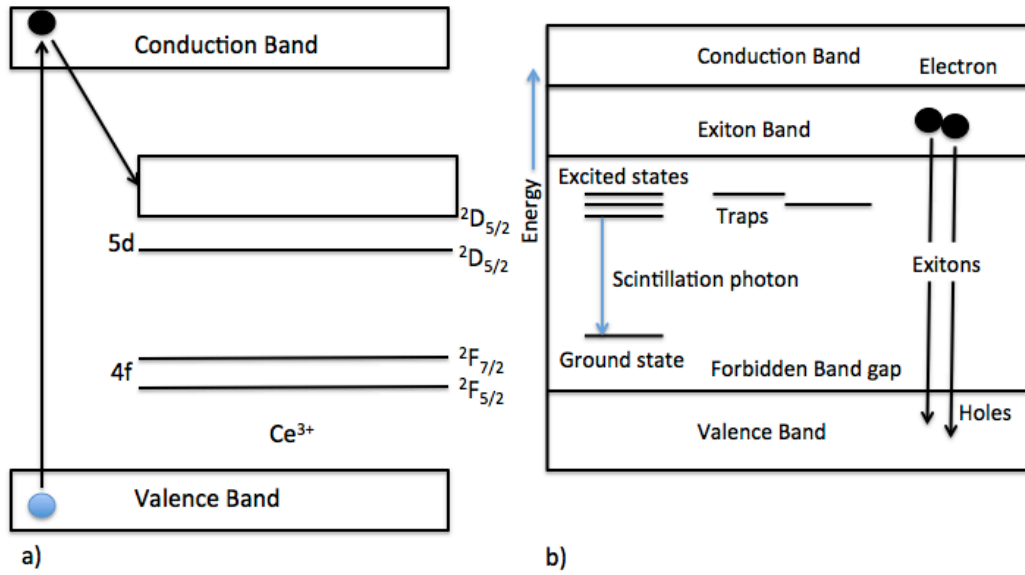
Figure 6.   (a) A schematic representation of the energy levels of the 4f and 5d configurations of Ce3+, responsible for the luminescence in lanthanum halide scintillators. (b) A diagram showing the typical electronic band structure found in scintillators. Adapted from [12].

If the energy of the excited electron exceeds the forbidden gap energy, thermal releases (phonons) can allow the electron to de-excite to an allowable photon energy release at a recombination site. Note, in some scintillators (i.e., BGO) there are no added activators like in the case of lanthanum halide crystal luminescence center shown in Figure 6, and they are considered self-activated. Often, these luminescence centers are doped with a material like Ce^+ because of its favorable photonic emissivity, due to its lower band gap. This is similar to a p-type semiconductor in that the positive charged ions with a low band gap allow recapture at energy levels where visible light can be emitted [11]. Regardless of emission, the next step of counting these light emissions is a challenge met with PMTs.

5.   Photon Counting

PMTs allow us to detect the photonic signal received from the scintillator by turning scintillation photons into electrical signals that can be measured. Figure 7 shows a basic schematic of a PMT and how it works.

10
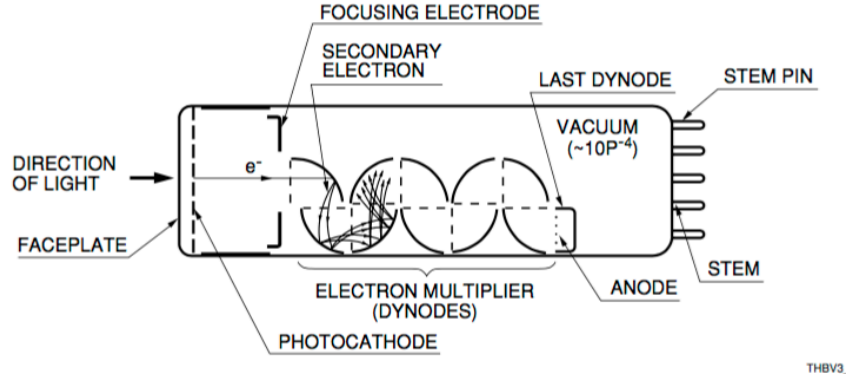
Figure 7.   PMT diagram. Source: [14].

In Figure 7, incident light hits the photocathode, through which the photoelectric effect, an electron is emitted, as long as the energy is enough to exceed the vacuum level barrier [14]. The photocathode is usually a semiconductor, and in this research GaAs was the semiconductor used the most. In Figure 8, there is a pictorial representation of how the incident energy must exceed the vacuum layer before it can be multiplied.
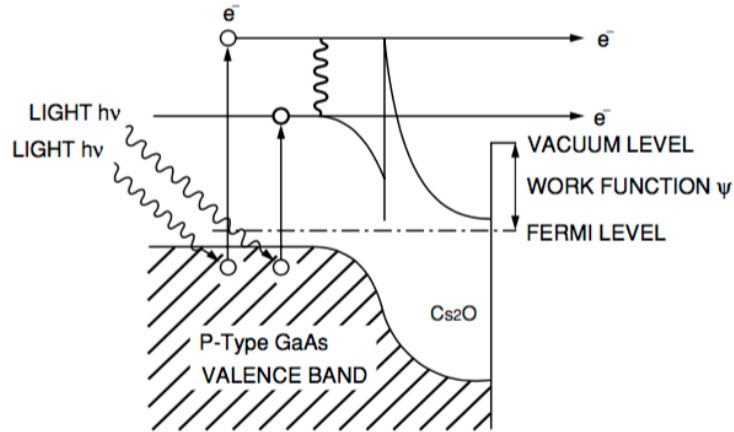
Figure 8.   Photocathode energy band structure. Source: [14].

The quantum efficiency of the detector is a ratio of output electrons to incident photons at the photocathode, and is given by [14]:

$$\eta(v) = (1 - R)\frac{P_v}{k} \bullet (\frac{1}{1 + 1/kL})$$

(4)

In equation (4), according to Hamamatsu:

11

R is reflection coefficient, k is full absorption coefficient, P_ν is the probability that light absorption may excite electrons to a level greater than the vacuum level, L represents escape length of an excited electron once an electron has escaped the photocathode into the vacuum, and ν is the frequency of light [14].

After the photocathode emits an electron, the next step is to use electromagnetic fields to focus the electrons on the dynodes, which multiply the electrons with secondary emissions until the last dynode, called an anode. The multiplication is typically ten to 100 times the initial number of electrons generated [14]. The voltage difference between the first dynode and last anode gives a signal that will be used to measure the intensity of the incoming light. Often this voltage difference is measured in pulses as each pulse represents one photon [14].

When conducting experiments with PMTs, it is important to reduce the dark current signal from the PMT, which is the current in the PMT tube in dark conditions. According to Hamamatsu, the contributors to dark current are:

1. Thermionic emission current from the photocathode and photodiode.

2. Leakage current (ohmic leakage) between the anode and other electrodes inside the tube.

3. Photocurrent produced by scintillation from glass envelope or electrode supports.

4. Field emission current.

5. Ionization current from residual gases.

6. Radiation, cosmic rays, environmental gamma rays [14].

The biggest problem encountered in this study was thermionic emission, which required the PMT to be cooled in some way. Hamamatsu does manufacture cooling systems that house a PMT and cool them to about -30^oC [14]. The reason for thermionic emission has been studied by W. Richardson and is characterized by [14]:

$$i_s = AT^{5/4}e^{(-e\Psi/KT)} \tag{5}$$

In this equation, T is absolute temperature, K is the Boltzman constant, e is electron charge, A is a constant, and Ψ is the work function [14]. As seen from equation (5), as

temperature increases, thermionic emission probability increases. Figure 9 illustrates how certain anode dark counts are affected by changing temperatures exponentially. In PMT measurements, the lower the dark count the better because the noise level can be easily differentiated from the light signal measured.
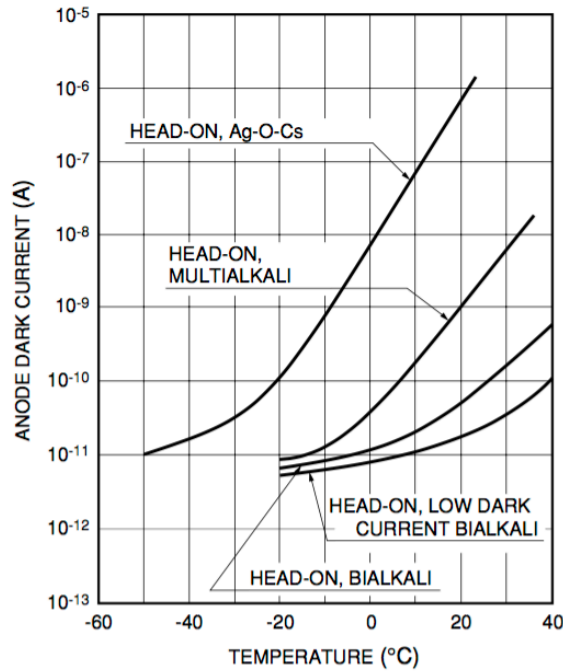
Figure 9.   Dark count vs temperature for select materials. Source: [14].

For reference, the anode material used for this study was mainly Cu-BeO, which corresponds to the third curve from the left.

It may be clearer now that in order to understand the physics of scintillators and how they react, one needs a background in nuclear technology and the processes of inelastic scattering, scintillation, and photonics. From the fission of the neutron to the detection of light by the PMT, one can understand how a scintillator can be used to detect fissile nuclear material. The intrinsic properties of nuclear weapons material, and the propensity of the neutrons resulting from their fission to inelastically scatter, defines the interactions of interest within scintillation crystals that can be read and understood.

Inelastic scattering is the process in which fast neutrons interact with scintillator crystal structure to emit gamma photons, which result in ionization events that ultimately

13

excite the scintillation material and cause their emission of photons of visible light. After these ionization and photon emission events, a signal difference in voltage develops into a PMT signal that can be measured.

To summarize, **the main objectives of this research were twofold: (1) characterize and delineate the interactions between the radiation and the scintillator, as well as the scintillation response to gamma and neutron interactions, and (2) create feasible testing apparatuses necessary to achieve accurate measurements of scintillator crystal response.** Although previous research has included studies of scintillation of heavy inorganic oxide scintillators, the physics behind the scintillation processes is known to be complicated and in some cases is still not well defined. An improved understanding of the physics of the response of these scintillators to gamma and neutron radiation is an important need.

B.   REMAINING CHAPTERS

The remaining chapters further discuss heavy oxide inorganic scintillators and the experimental results using select crystals. Chapter II covers scintillator types, along with a short discussion of the scintillators used in experiments conducted in this research. Two of the three experiments discussed in the following chapters were created from scratch, therefore they are described in detail for future use and discussion in Chapter III. Of the two experiment apparatuses, one is primarily focused on peak emission while the other is a portable photon counting experiment creation. Chapter IV discusses the types of experiments completed and provides an in-depth look at the results of each experiment. The first set of experiments used gamma radiation for crystal excitation, and the last experiment was based on neutron source excitation. The experiments start from the basic understanding of each crystal's performance and a comparison to each other with an in-depth look into why each crystal performs better or worse. Then, in order to understand and study emission response of all the scintillator crystals, a second set of experiments was completed with a Photo Counting Spectrometer (PCS). The final set of experiments focused mainly on fast neutron interaction and response. Chapter V completes this research analysis with some final thoughts and recommendations for future study.

However, in the next chapter we describe the crystals that are available for testing and the basic characteristics of each crystal and why they differ from other known scintillator crystals.

THIS PAGE INTENTIONALLY LEFT BLANK

II. SCINTILLATOR CHARACTERISTICS

A. TYPES OF SCINTILLATORS

Scintillators are used in a variety of applications, however the focus of this research is radiation detection and measurement and, in particular, detection of fast neutrons using heavy inorganic scintillators. The selection of a proper scintillator depends on the intended application, as scintillator characteristics are variable. The response of a given crystal is largely based on its chemical composition, dopants, and crystalline structure. In this research, the crystals used were heavy oxide scintillators, selected primarily for their potential ability to enhance the occurrence and detection of neutron inelastic scattering while also responding to other neutron-matter interactions. Regardless of their characteristics, scintillators are reliable in radiation detection measurements and can be effective in passive radiation detection.

According to Rodnyi, there are four categories of solid inorganic scintillators: halides, oxides and oxide systems, chalcogenides, and glasses [11]. Typical Halides are alkaline earth fluorides, alkaline halide crystals (AHCs), and bi-cation halides. What is interesting with halides is that BaF_2, an alkaline earth fluoride, is particularly good at neutron detection with gamma background. This would be particularly useful for reactor neutron detection or radiation disasters where there is a high gamma concentration. Oxides are best known by their high thermal chemical and radiation stability, and chalcogenides are known for their radiation hardness [11]. Glasses, which are used for many applications, are simple and cheap [11]. In this research heavy oxide scintillators were used in all experiments.

The Institute of Scintillator Crystals (ISC) in Ukraine has a long history of developing scintillator crystals for a broad range of applications, and has actively explored heavy oxide inorganic scintillators for high-efficiency detection of fast neutrons. Because of collaboration with this institute, we were provided with a selection of crystals fabricated by ISC for purposes of this research described in Table 1.

Table 1.   Heavy oxide scintillator crystals obtained from the Institute for Scintillation Materials, Ukraine. Adapted from [11], [15]–[18].

Crystal	Chemical Formula	Acronym	Dimensions (mm)	Z_{eff} Ranking	Band Gap (eV)	Crystal Structure	Density (g/cm^3)
Bismuth Germanate	$Bi_4Ge_3O_{12}$	BGO1	20x30x11	1	2.46	Volume Centered Cubic	7.13
Bismuth Germanate	$Bi_4Ge_3O_{12}$	BGO2	20(dia)x10 (cylinder)	1	2.46	Volume Centered Cubic	7.9
Lead Tungstate	$PbWO_4$	PWO	20x20x10	2	2.95	Sheelite Structure	8.28
Cadmium Tungstate	$CdWO_4$	CWO	20x20x10	4	2.54	Wolframite Structure	7.9
Zinc Tungstate	$ZnWO_4$	ZWO	20x20x20	3	2.59 1.4-2.0 (ZnO)	Wolframite Structure	7.9
Lutetium-Gadolinium Orthosilicate	$Lu_2Gd_2SiO_5$ (Ce .3%))	LGSO	20(dia)x10 (cylinder)	5	2.96 (Ce) 3.88 (LuAlO)	Monoclinic	7
Lutetium-Aluminum Garnet	$Lu_3Al_5O_{12}$ (Ce .001%)	LUAG	20(dia)x10 (cylinder)	6	2.49	Cubic	6.73

In Table 1, the Z_{eff} ranking is based upon bulk density and Z number, which should correspond loosely with probability of interaction without delving into interaction cross sections, absorption coefficients, and neutron cross sections. This probability of interaction is described in Chapter I and Figure 5. Notice how BGO should generate the highest light output based upon this ranking by probability of interaction. This was of particular importance in later parts of this study, when trying to understand why some crystals exhibit stronger scintillation than others at the same intensity and energy level of incident radiation. The crystal structure and density are also listed because they are of particular use to characterize why some crystalline responses are more prominent with similar crystalline structures or similar densities. An example of cadmium tungstate (CWO)'s crystalline structure is displayed in Figure 10.
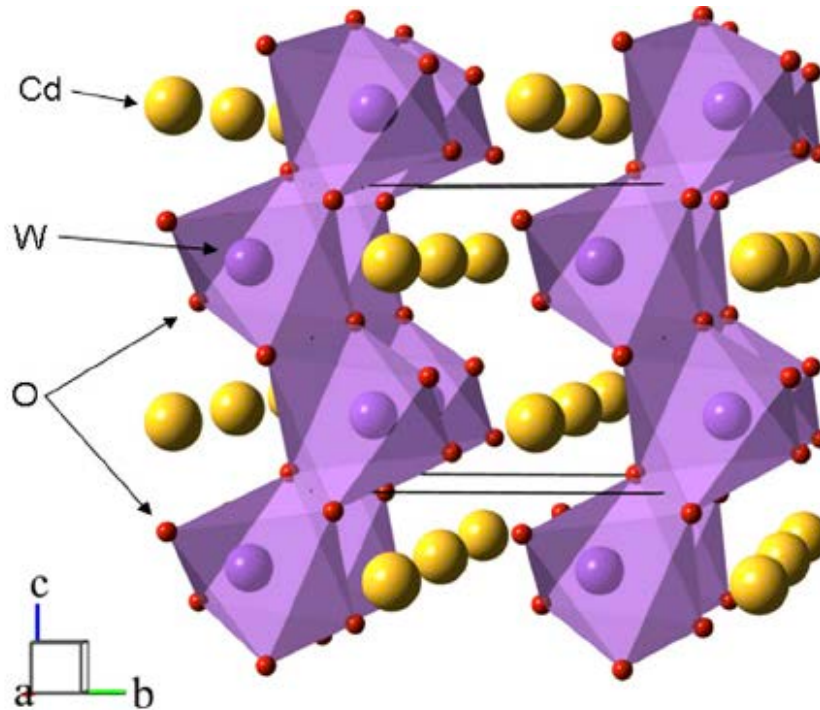
Figure 10.   CWO wolframite crystalline structure. Source: [19].

Notice that the crystalline structure of the tungstate, according to Grinyov, "is where each Oxygen and Tungstate is surrounded by a distorted octahedron of oxygen atoms" [15]. The Oxygen and Tungstate portion of the crystal combined have a particularly large Z number, which can contribute to the capture of the incoming radiation when combined

with high density. Of the four types of scintillators described briefly, the heavy oxides listed in Table 1 provide plenty of insight on scintillator crystal response. Response is what is primarily measured and analyzed in this research, as defined by the amount and type of light a particular crystal emits when exposed to different radiation sources. First however, there must be some discussion of how this light response is measured.

B.   PHOTONIC RESPONSE

The photonic response of a scintillator is measured in scintillation yield or L_R [11]. Yield is calculated as equation (6) with units of photons/MeV [11].

$$L_R = \frac{N_{ph}}{E_\gamma}$$ (6)

In equation (6) E_γ is energy deposited and N_{ph} is the photon count. This response is comprised of 4 main types of luminescence: core-valence luminescence, extrinsic luminescence, intrinsic luminescence, and afterglow (phosphorescence) [11]. Core-valence luminescence is due to a radiative electronic transition between the valence band and the outermost core band [20]. Intrinsic luminescence is due to self-trapped exitons, due to defects or other core excitations, emitting energy based upon the natural crystalline characteristic of the crystal [11]. The photon release can be in the visible range, but it depends upon where the recombination takes place, which is sometimes not at the luminescence center. Extrinsic luminescence is due to excited luminescence centers, after excitation of energy and recombination discussed previously in Chapter I. Phosphorescence originates from defects in the scintillator and free valence exitons [11]. In this study the main focus is on extrinsic luminescence for measuring scintillation yield as it is the predominant mechanism for radiation-induced scintillation measurements.

On a fundamental level, heavy oxide scintillators provide interaction sites for inelastic scattering (as well as other neutron interactions) which result in direct ionization as well as gamma radiation emission. Two-thirds of this study focused on scintillator response to gamma radiation above 2.5 MeV, which is a good simulation of scintillator response to high-energy neutrons after recoil and emission of gamma radiation. Gamma

radiation from Co-60 after reaction with the scintillator crystal will ionize the material to create e-h pairs, that when recombined produce scintillation. PMTs will be the instruments of choice for recording photon counts allowing the determination of light yield. According to Rodnyi, the measurement for photon yield is limited by the band gap of the crystal [11]. According to equation (7), the maximum photon yield/MeV (L_{max}) increases as band gap (E_g) decreases [11].

$$L_{\mathbf{max}} \approx \frac{.5}{E_g} \times 10^6 \left[\frac{photons}{MeV} \right] \qquad (7)$$

However, this equation assumes that the number of photon counts is equivalent to the number of created e-h pairs [11]. Therefore, this is a rough approximation for the heavy oxide scintillators used in this research.

Although scintillators are used in a variety of applications, the focus of this research is in radiation detection and measurement, specifically fast neutrons from nuclear materials. As expected, the selection of the scintillator depends on the application. The effectiveness of detection is based upon a variety of factors as each crystal has its own unique composition and band structure. Regardless, the scintillation of all heavy oxide scintillator crystals in this study was studied after exposure to available radiation sources.

The next section will detail how most of the testing apparatuses were built to measure photon yield from the heavy oxide scintillators given. The first experiment apparatus is a photon counting spectrometer. The second apparatus creation was devised as a means to conduct a relatively simple experiment in a portable medium capable of measuring a significant radiation signal without an expanded setup and calibration. Both of these apparatuses were used to test scintillator crystal response to gamma radiation, and the portable apparatus was additionally used for detection of fast neutrons. The details of the experiments completed are included in Chapter IV.

THIS PAGE INTENTIONALLY LEFT BLANK

III. EXPERIMENTAL APPARATUSES

A. EXPERIMENT GENESIS

A considerable amount of time and effort was made to develop two of the three experiment apparatuses used in this research in order to create the settings required for two distinct results. The first setup, was built from scratch using a decommissioned Scanning Electron Microscope (SEM) because there was no other Naval Postgraduate School locally available Photon Counting Spectrometer (PCS). Although photon counting with a PMT provides useful data, it does not provide the spectral characteristics of the scintillators. The second experimental apparatus was created using a silicon femtowatt photoreceiver in a light tight box, portable and capable of counting photons after exposure to fast neutrons without significant cost or pre-experiment setup. This was necessary in order to perform the measurements rapidly where the neutron sources were available. Regardless, the genesis of both apparatuses began with a necessity to detect scintillator output beyond just photon counts conducted in the first experiment setups described in Chapter IV.

B. PHOTON COUNTING SPECTROMETER

1. Background/Instrumentation

The first apparatus built was a manifestation of an old deactivated JEOL 840A SEM with an Oxford MonoCLII attachment. The combined system was available to conduct wavelength experiments, but the electron beam was no longer operational. Additionally, the system did not have the specifications or manuals necessary for basic use. Furthermore, all of the instrumentation to record and conduct experiments with the device were not in operational condition. Attached to the Oxford MonoCLII was a C2761 Hamamatsu PMT cooler, which housed an R943-02 PMT tube. The PMT has a maximum quantum efficiency of 14% with a spectral range of 160-930nm with a gain of 5×10^5 [21]. The PMT cooler cooled the PMT using a Peltier thermoelectric cooler, with electromagnetic shielding to improve the dark count. The cooler cooled the PMT to a maximum controlled setting of -30° C. However, as previously stated, the instrumentation

and power supply for the SEM system was not readily active or available so the entire measurement system for data collection needed to be created. Once power is applied the PMT, the output voltage signal can be measured, but how photons are captured by the PMT is a complex process that needs elaboration.

The Photon Counting Spectrometer (PCS) has two main functional settings within the monochromator that are set using the two knobs on the monochromator knob display. The monochromatic setting is the most complex function as is shown in Figure 11.
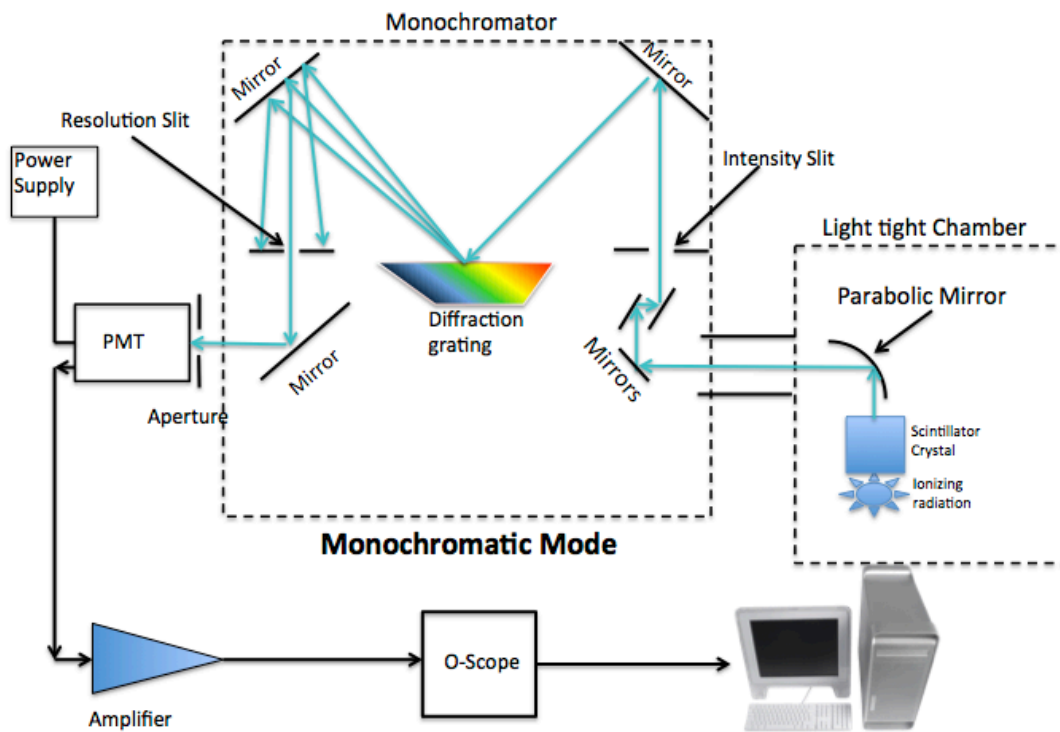
Figure 11.   Monochromatic mode block diagram of PCS with light emitting scintillator crystal.

As shown in Figure 11 after a light source emits light, the parabolic mirror directs that light to a set of mirrors which channel the light to the diffraction grating, where the light is then re-directed using a second set of mirrors into the PMT aperture window. The signal is amplified using an SR560 and then sent to an Agilent Technologies MSO-X 3054 Oscilloscope. In the panchromatic setting all light captured by the parabolic mirror shown in Figure 12, goes directly into the PMT capture window.
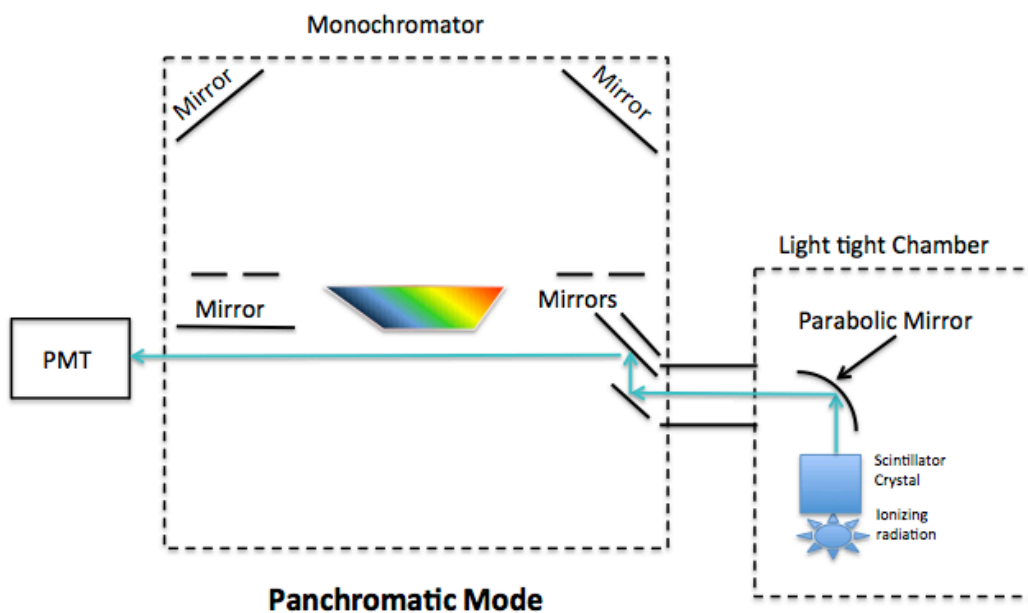
Figure 12.   Panchromatic mode block diagram of PCS with scintillator crystal
and ionizing radiation

The two knobs that control the panchromatic and monochromatic settings control the two monochromator mirror settings shown the left and right of the diffraction grating. The schematic diagram of the instrumentation is shown in Figure 11, and Figure 13 shows the actual experiment setup.
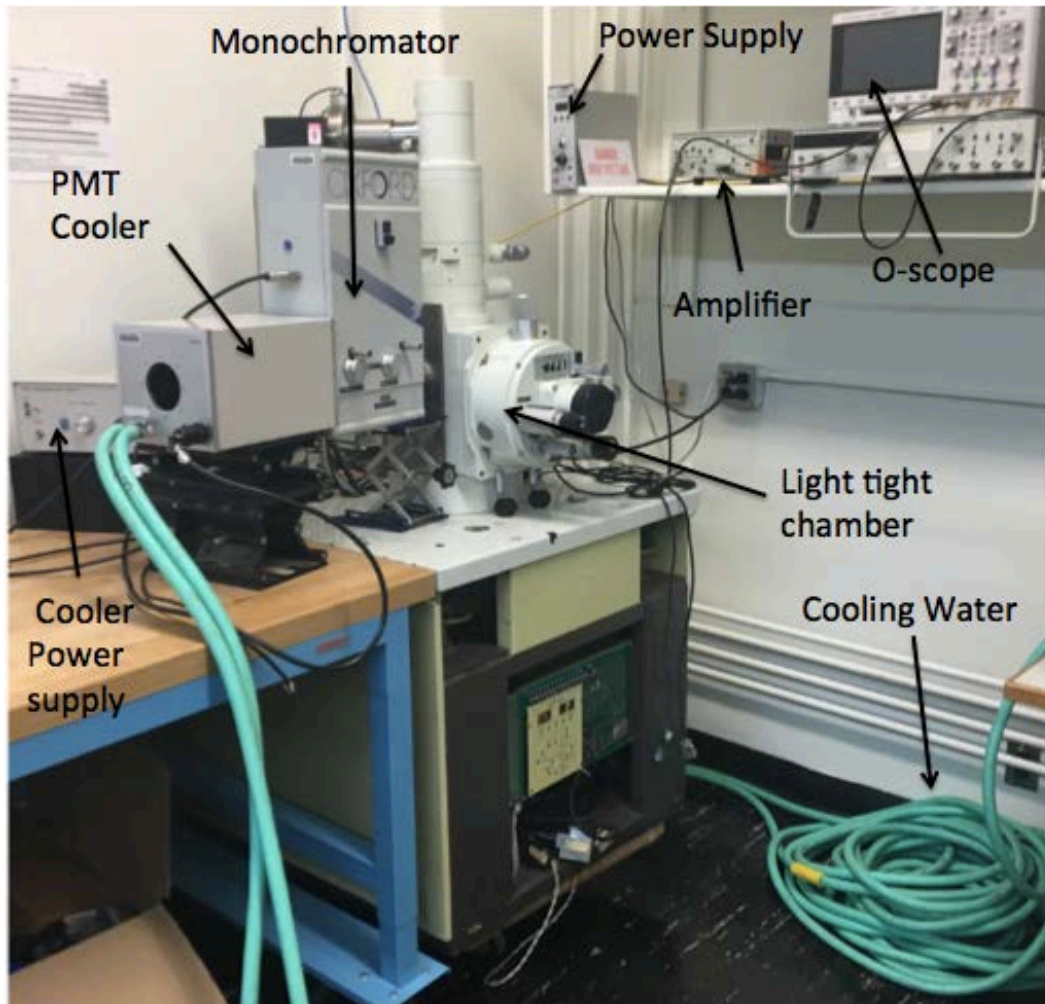
Figure 13.   Spectroscopy measurement setup.

For further description of light capture, Figure 14 is a detailed ray tracing diagram, that describes the process in which light first gets captured and guided, until it is measured by the PMT and read as an electric signal. The Oxford MonoCLII is in the center of the diagram and has several control knobs which allow one to manually control specific settings in the diffraction grating chamber shown in Figures 11 and 14. The top knob has four digits and manually controls the diffraction grating which consists of 1000 lines. Below the top knob are the two resolution slit knobs which can be adjusted to increase or decrease the spectral resolution. The slit to the right controls the intensity entering the chamber and the slit to the left controls the spectral resolution. Below these knobs are two additional knobs used to set the device to monochromatic, or panchromatic

26

mode. There is a series of mirrors that reflect the incoming light off the diffraction grating, in a monochromatic setting and focus the light into the PMT window. How this occurs is described in Figures 11 and 14.
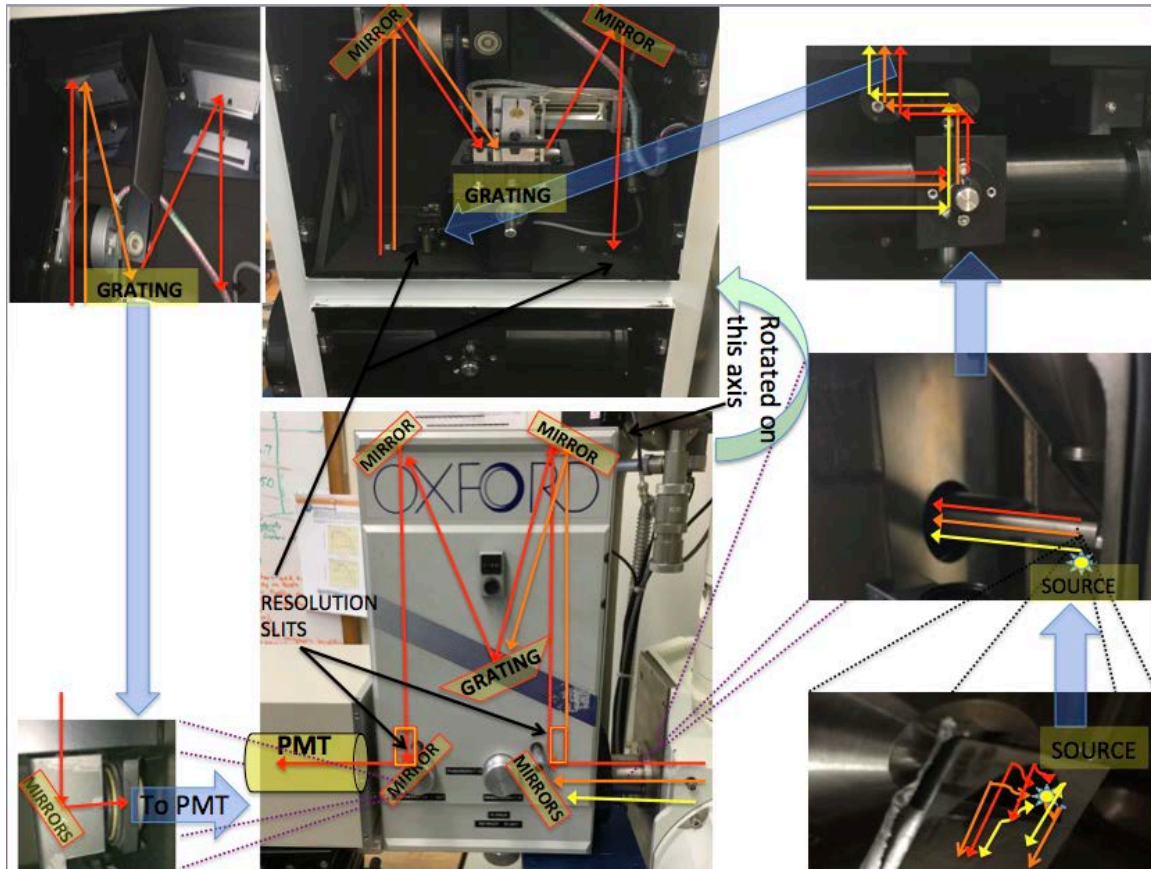
Figure 14.   Pictures of monochromator with light rays emitting from a source directly underneath the parabolic mirror.

In Figure 14, starting from right to left, if a source is placed in the SEM chamber, the light emission from the source is captured by a parabolic mirror and reflected as collimated light into the first set of flat mirrors, which, depending upon the panchromatic or monochromatic setting, reflects the light into either the PMT window directly or into the monochromatic chamber. Both knobs on the front of the MonoCLII, need to be set to panchromatic, for the second mirror in the chamber to turn and reflect the light into the PMT window. Figures 11 and 14 trace the light rays for the monochromatic setting only. When both knobs are set to monochromatic, then the diffraction grating and complex

optics come into play. As shown in Figures 11 and 14, on monochromatic mode, the light first enters the chamber after going through the intensity control slit. This slits can be adjusted to reduce the amount of energy that enters the chamber. More testing needs to be done to calibrate these knobs for accuracy. After entering the chamber, the light reflects off the first mirror going towards the diffraction grating for wavelength discrimination. The light dispersed by the grating reflects off the second mirror, passing through the resolution slit, which emits the spectral portion that goes to the final mirror, and then into the PMT window.

However, in order to get to the final product shown in Figure 13, several instrumentation steps had to be done within several months. The Hamamatsu 943-02 PMT power supply is a TC 952A Tennelec High Voltage Supply while the C2761 power unit controlled the PMT Cooler. Once power was applied, the voltage signal from the PMT was collected using a MSO-X 3054 Oscilloscope. The settings on the oscilloscope determine the time frame and frequency of measurements, detailed in Chapter IV. Figure 15 is an illustration on how noise was differentiated from photon counts on the Oscilloscope.

Figure 15.   Oscilloscope reading example.

After powering up the PMT with 1500 V, the first measured dark count for this system was 4×10^6 counts/s, with the lights in the lab on; this was much too high of a background to conduct accurate measurements. Typical dark counts specified for the PMT ranged from 20–100 counts/s if cooled to -30° C. Although the cooler was attached and running, it did not have water flowing through the thermoelectric Peltier cooler. After several failed attempts of attaching a water chiller, a nearby sink was taken apart and a hose was clamped above the water shut-off valve. The typical water temperature from this valve is about 20° C, which is well within the operational range of the cooler [22]. However, if the water pressure was to exceed 3 kg per cm^2, water leaks would develop inside the cooling unit [22]. The flow rate was measured from the hose and adjusted to be below 0.79 Gal/min., which would not exceed the specification of the cooler. In order to repeat this process, the turn radius on the water shut-off valve was marked so any user can move to that setting to reach and not exceed 0.79 Gal/min. After several iterations to determine the best setting on the oscilloscope, the dark count was reduced to 5–40 counts per second with the lights off and up to 100 counts/s with lights on. The next step after acquiring a signal was to get to a point to where the signal could be analyzed.

Single photon response without the original software and instrumentation was difficult, but accomplished by combining several instruments on hand. After power was applied the signal was first amplified with a Stanford Research Model SR560 Low-Noise Pre-amplifier with a gain of $2x10^2$ setting displayed on the SR560 display window with a low noise mode applied. Filter cut-offs available on the SR560 were not used in this setup. After this amplifier was attached and power was applied, the oscilloscope provided a running visual picture of the pulse counts, but did not allow one to get an accurate picture of average counts. Labview was used to count the signals on the oscilloscope screen and then averaged out. The noise level displayed on the oscilloscope at 2000 V supplied to the PMT ranged from 0 to - 0.029 V. Labview was used to filter out this noise level and count pulses above this threshold value. Signal measurement was performed by measuring the pulse count above a threshold value set in Labview, preferably above the noise level as shown in Figure 15. For example, a signal threshold setting selected in the program can read from 0.29V-15 V and every pulse above 0.29 V would be recorded as one photon. The time for the counts recorded depends of the time set on the Oscilloscope. Additionally, the frequency of each timeframe snapshot is indicated in the Labview software as number of runs. For example, in Figure 15 a 10 m/s duration is selected, if 10 runs is set in the Labview program, then the program will capture 10 occurrences of a 10 m/s snapshot and average those ten intervals and record that count average and the wavelength position of the diffraction grating. Once this setup was complete, the entire apparatus was ready to be used to conduct experiments. However, the next requirement was to calibrate the completed setup to ensure accuracy.

In order to place the scintillator in the right place, optically speaking, the focal point of the parabolic mirror had to be determined. For that, the PMT was removed from the cooler and a collimated light beam was placed in the housing, close to window of the Mono CLII. This calibration setup is shown in Figure 16.
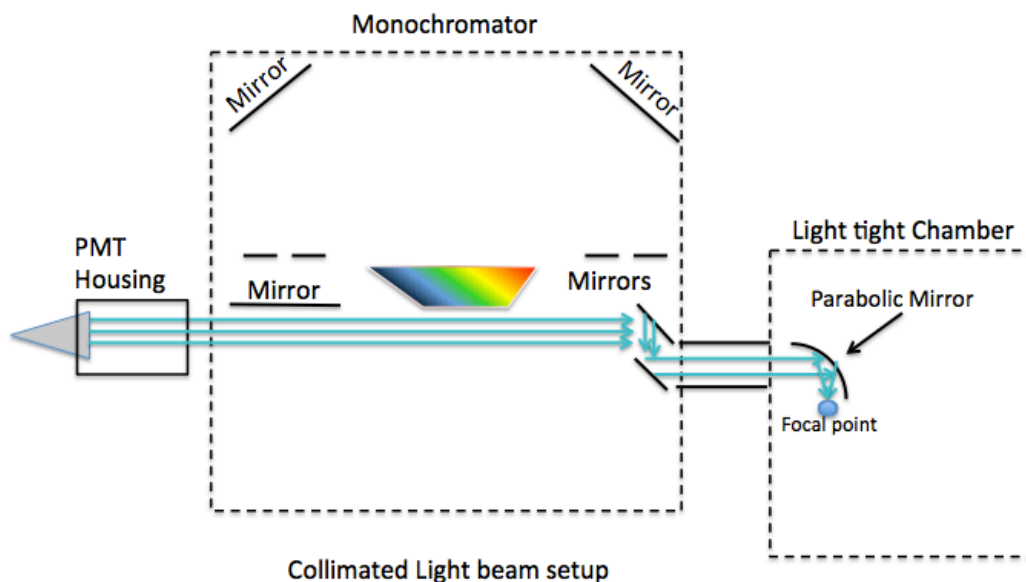
Figure 16.   Collimated light beam setup used to determine to focal point of mirror

The MonoCLII parabolic mirror focused a beam of light approximately 0.5 mm below the mirror surface plane. From this point one can move the X, Y, and Z adjustment settings on the JOEL 840 to get a maximum signal. Note that the X, Y, and Z settings vary depending upon the mount used which is a factor of the height and depth of the sample being tested. After the focal point was found, the calibration of the experimental setup performed using a Hamamatsu 11494-525 1 pW LED.

2.   PCS Calibration

Continuing from the focal point discovery, a Hamamatsu 1 pW L11494-525 LED light source was chosen to finally calibrate the setup. According to Hamamatsu, the peak emission of the 1 pW LED is 522 nm and the spectral characteristic is shown in Figure 17 by the solid green line [23]. In order to perform the calibration, the water flow rate was measured at 0.62 Gal/min and the C2761 cooler was turned on to cool the PMT 2 hours before any measurement. The signal threshold was set to .029-15 V and the resolution slit on the MonoCLII was set to 2.0 mm. The SR560 was set to 2×10^2 and the LED light was set on a mount that was 10.92 mm high and placed at the focal point of the parabolic mirror. Maximum signal was generated with a setting of X=9.25, Y=16.46, and Z was not

31

adjusted out of fear of contacting the parabolic mirror. Aluminum was set to cover the hole on top of the parabolic mirror to reduce light loss. At 2000 V and the PMT Cooler set to maximum cooling, the dark count averaged 39.6 counts/s after 100 runs. After the 1pw source was turned on, the PMT measured 782.25 counts/s in panchromatic mode with a 100 counts/s dark count. From this point, the wavelength was adjusted manually in 5 nm increments from 440 nm to 630 nm. The exact setup described previously was repeated with a count of 740 counts/s in panchromatic mode with a 57.35 counts/s dark count. The data was analyzed and graphed using Matlab, and the results are shown in Figure 17.
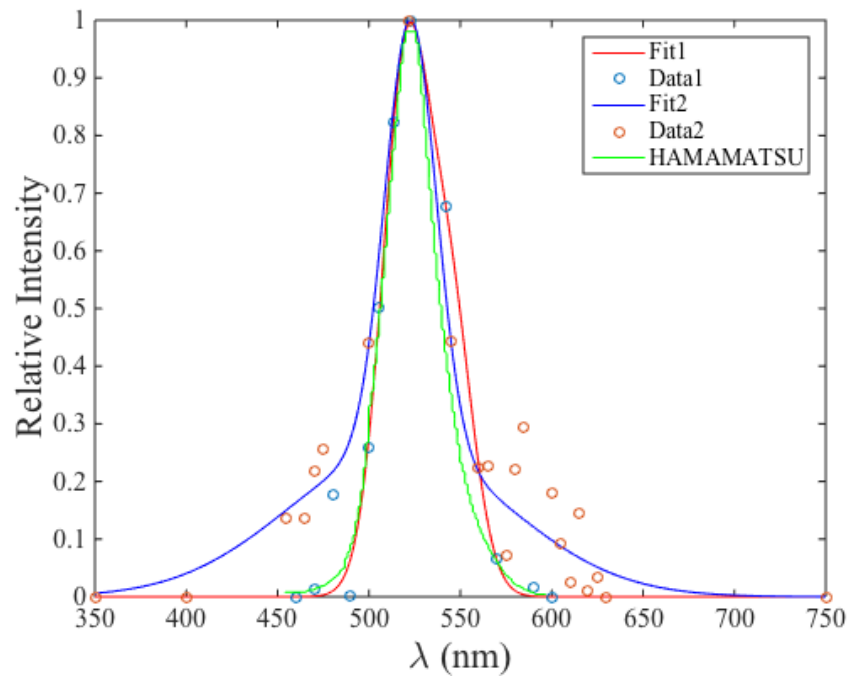
Figure 17.   Peak emission data of Hamamatsu 11494-525 with data fits for calibration of PCS .

Figure 17 shows the results from the two tests, Gaussian fitted and graphed with the data from the 11494-525 data sheet. The good agreement between the provided and measured spectral responses is enough to validate the PCS. While the peak emission wavelength published by Hamamatsu was 522 nm, the graphed data shows a range of peak emission of 522 nm to 525 nm confirmed by each test shown as the blue and red lines. At this

point, the setup created from scratch was ready to be used with scintillator crystals to measure the peak emission from each crystal after exposure to radiation. LGSO was the first crystal tested due a strong expected strength of signal. The results for this experiment are detailed in Chapter IV. Unfortunately, the posi-drive belt failed and had to be repaired before this apparatus at this specific calibration could be used for additional measurements.

3.   Re-Calibration

After a new posi-drive belt was installed, as shown in Figure 18, a second calibration procedure was used to ensure the belt installation did not cause any error, and the system was automated with Labview, thanks to the programming of Jeffrey Catterlin, research assistant of the Sensor Research Lab.
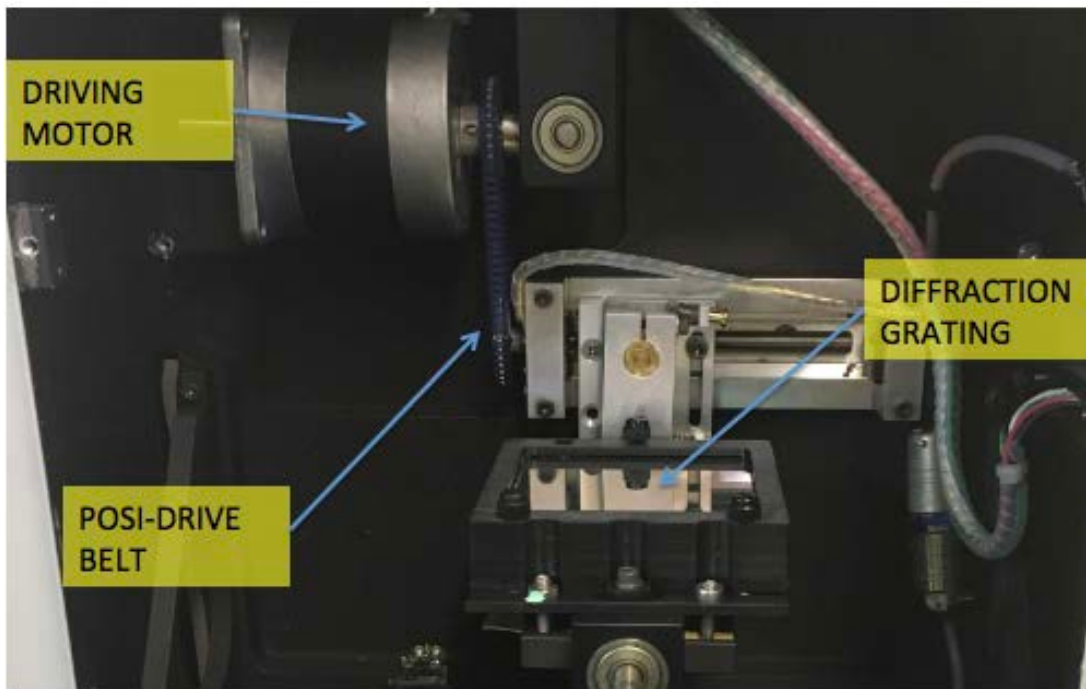
Figure 18.   Posi-drive belt location inside MonoClII.

Lasers were used to assist in the wavelength calibration of the device once the posi-drive belt had been removed because there was not a definite way to ensure that the position of the diffraction grating corresponds to the indicated value in Labview. Additionally, care

had to be taken to ensure that as the diffraction grating moved, it moved in correlation to the wavelength input on the program, which accounted for backlash. HeNe Lasers of 632.8, 543, and a 432.8 nm laser pointer were aimed through the PMT window and aligned with the resolution slits until so that the reflection from the diffraction grating wavelength line corresponded to the wavelength of light emitted by the laser. Here is where it was noted that 0.5 mm on the selection knob loosely corresponds to wavelength plus or minus 10 nm. By this is meant that the output of laser light after diffraction from the monochromator focused a beam spread onto the resolution slits that corresponded to a selection of 0.5 mm. Therefore, since the lasers were accurate to plus or minus 10 nm, it was assumed that 0.5 mm on the selection knob corresponded plus or minus 10 nm. In Figure 19, the wavelength calibration diagram setup is shown with the 543 nm laser. This setup is similar to the setup described in Figure 16 except HeNe lasers were used instead of collimated white light.

Figure 19.   HeNe Laser calibration after posi-drive belt installation.

After the calibration, the Hamamatsu 11494 was placed in the chamber and the system was re-tested to verify that the setup can still accurately detect peak wavelength emission. The source was centered at Y=10.6 and X=20.0, giving a 744 count/s reading

in the panchromatic mode with a 120 count/s dark count. The oscilloscope was set to 10 m/s per division before 2000 V was applied to the PMT. The threshold for capture was set from 0.15-15 V and the SR560 was set to low noise with a 1×10^2 gain, DC coupled. The dark count could not be differentiated from the signal at resolution slit setting of .5-2 mm so both resolution slits were opened to 5 mm to maximize the signal. The results shown in Figure 20 show that the re-calibration was very successful considering all of the possible errors that could have been made in putting the MonoClII back together.
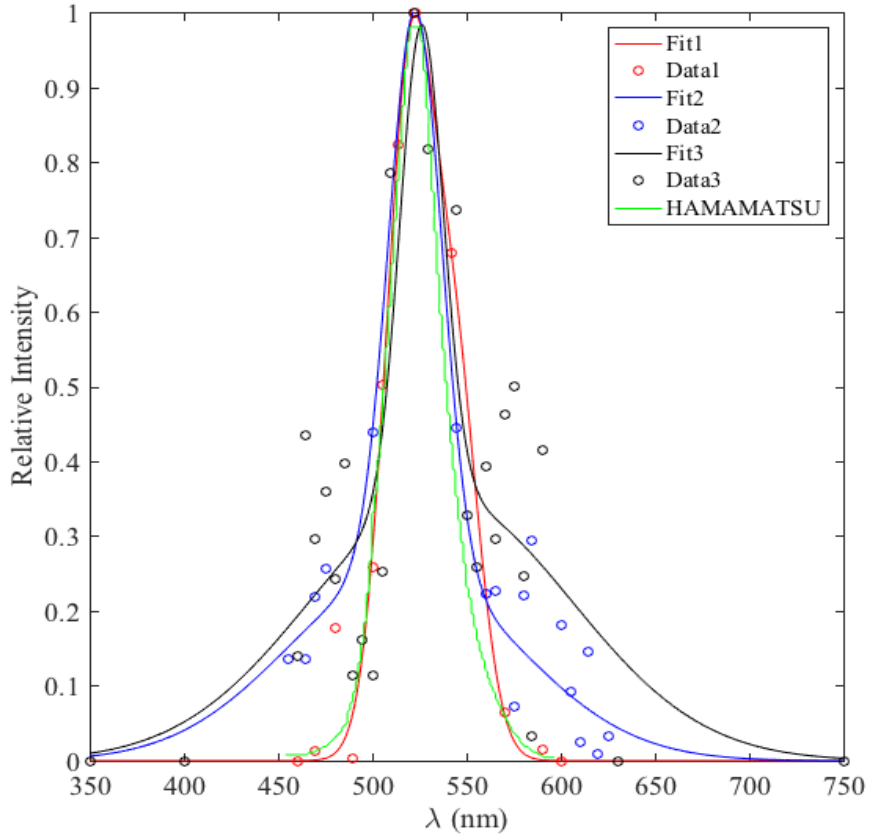
Figure 20.   Re-calibration of PCS with Hamamatsu 11494-525 LED

In Figure 20, the black solid line represents the spectral relative intensity of the 1 pW LED after re-calibration. When compared to the previous results, the peak emission is less than 3 nm off from the previous calibration, but less than 1 nm away from the peak emission published by Hamamatsu [23]. Therefore, the PCS was considered accurate to perform spectroscopy on the scintillator crystals of interest.

C.   LIGHT TIGHT CHAMBER WITH FEMPTOWATT PHOTORECEIVER

Although the PCS is efficient for low intensity scintillation measurements, for obvious reasons it is not portable. Additionally, if the ultimate use of the crystals would be in portable detector device that is not bulky and expensive, this setup is not practical, nor does it prove the original synthesis of this research in that scintillator crystals could prove to be a viable candidate to reduce cost and increase efficiency in neutron detection. To conduct experiments with fast neutrons at different locations, a New Focus 2151 femptowatt photoreceiver, a portable solid state detector, was used inside a light tight chamber.

The enclosure was made of PVC, 6.33 mm thick, and is a cube approximately 1ft^3. The photoreceiver has 3 gain settings internal to the device and the 1mm diameter Silicon detector can detect small amounts of light in the 300-1050 nm range with a 9 V battery as the power supply [24]. In order to compute output voltage for a given input optical power, the following relationship in equation (8) is used [24]:

$$V_{out} = P_{in} \times R \times G \qquad\qquad (8)$$

Where P_{in} is the input optical power in watts, R is the photodetector's responsivity, and G is the amplifier's trans-impedance gain [24]. The responsivity profile for the detector is published in [24] and the responsivity used for calculations was assumed to be 0.3 A/W. From equation (8), given a measured output voltage one can solve for the input optical power and convert that into photons per second with equation (9):

$$P_{in}(photons / s) = \frac{V_{out}}{R \times G} \times \frac{\lambda}{h \times c} \qquad\qquad (9)$$

Where λ is the wavelength of the photon, h is Plank's constant and c is the speed of light [24].

The femptowatt photoreceiver was connected to a Fluke 87 multimeter to test light leakage into the enclosure. The readings showed that considerable light was leaking into the box. In order to reduce the background count further, electrical tape was placed along all the seams of the box where the rubber cement sealant held the box together.

Play-Doh was wrapped around the cords from the photoreceiver to plug the holes. These simple solutions reduced the dark count inside the box from 5 mV to below 4 mV. The light tight chamber with femtowatt photoreceiver (LTCFP) system cost approximately $1450.00, not including the amplifier. Cost estimates include a $995 photoreceiver, a $449 Fluke 87 multimeter, and PVC material that costs less than $30.00. However, the next step was to calibrate the device simply for future use similar to the PCS.

In order to calibrate the device, the 11494-525 Hamamatsu 1pW LED was used again, to measure the signal the LED generated in photons/second. The signal from the photoreceiver was amplified with the SR560 with a gain setting of 20 then averaged using a Fluke 87 multimeter set on high resolution. Overall, the measured photon counts were low when compared to the PCS. Average counts ranged from 24.49 counts/s to 43.8 counts/s compared to nearly 800 counts/s measures by the PCS. The number of photons was obtained by equations (7) and (8) after subtracting the dark count. However, an assumption was made that when the scintillator crystals were bombarded with fast neutrons, the crystals would generate a signal stronger than the LED that could be easily measured. Additionally, with the setup shown in Figure 21, measuring the scintillators' response to fast neutron excitation can be done without much preparation time or cost.
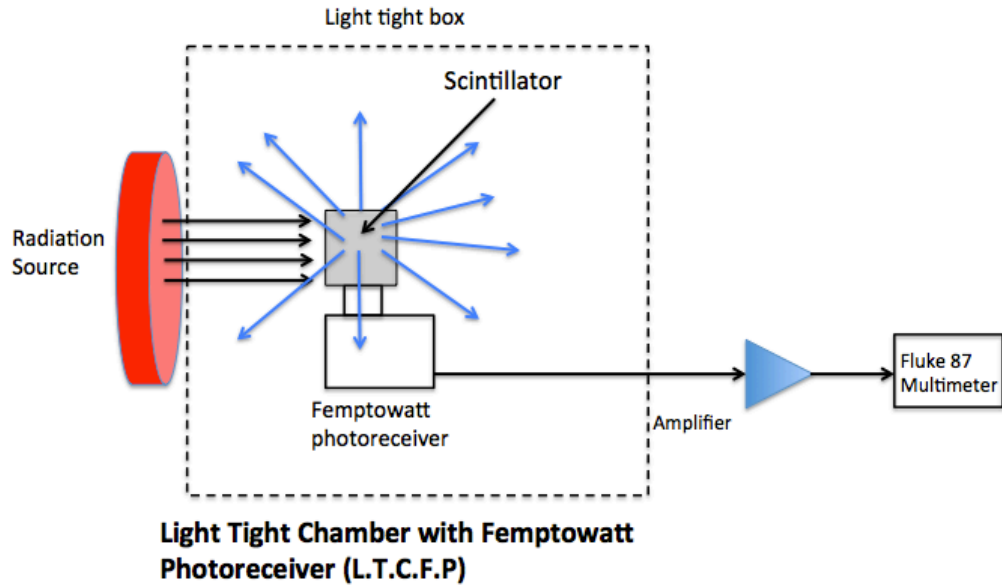
Figure 21.   LTCFP setup with instrumentation for portable experiments

The next chapter focuses on experimental results from these testing systems, but the first experiments were done with a PMT setup already established. The aforementioned apparatuses were not used until after the initial four experiments were completed. Regardless, both experiment creations were developed to improve upon the scintillator photonic response measurements to get a better understanding and characterization of scintillator response. To get a basic understanding of crystalline response a pre-established PMT set-up was used to test the scintillator crystals response to gamma radiation.

IV. EXPERIMENTAL RESULTS

A. PHOTONIC EMISSION-GAMMA INDUCED

The initial experiments conducted using the heavy oxide inorganic scintillators from Ukraine, were gamma-induced photon counting experiments using a Hamamatsu 7421–40 PMT. As shown in Figure 22, the radiation source was placed directly in contact with the scintillator crystal in front of the Thorlabs MAP104040-M achromatic lens pair. The 7421-40 Hamamatsu counting head was powered by a C9525 Hamamatsu Power Supply. The signal was sent to a C8855-01 Hamamatsu Photon Counting Unit and then amplified before being sent to the Computer in the adjacent room to be recorded.
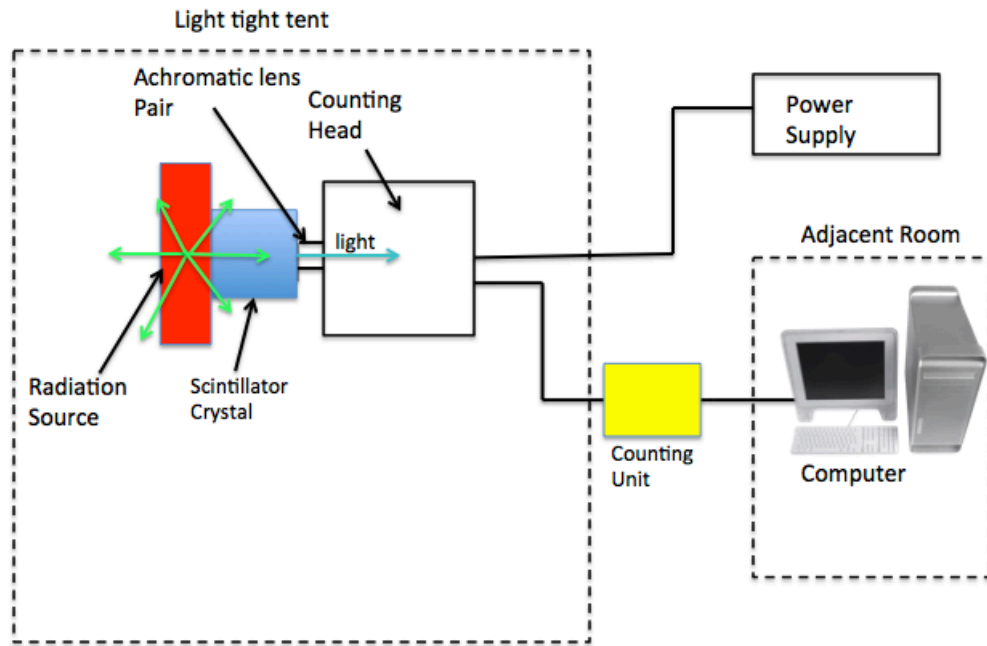
Figure 22.   Gamma radiation Hamamatsu 7421-40 counting head and dark room setup.

The PMT used a GaAsP/GaAs photocathode and a thermoelectric cooler, with high sensitivity for wavelengths from 300 nm to 720 nm and quantum efficiency of 40% at peak wavelength [25]. The PMT was placed in a dark room and the recordings were

analyzed after 3 minutes of gamma exposure per crystal. The dark counts were recorded without a crystal, with a crystal, with a source and with a source and a crystal.

1.   Method for Gamma-Induced Scintillation with 7421–40 PMT

All experiments were performed using a Co-60 source described in Table 2.

Table 2.   Co-60 Gamma source. Adapted from [17], [18].

	Co-60
Original Activity	1 uCi
Half-life (yrs.)	5.27
Energy (MeV)	2.5
Manufacture Date	October 2006
Thickness	3.03 mm
Diameter	6.77 mm

The decay of Co-60 is represented by [5]:

$$^{60}_{27}C \rightarrow ^{60}_{28}Ni + ^{0}_{-1}e + \gamma \tag{10}$$

Where Co-60 decays to Nickel-60 (Ni-60) by emitting two gamma rays of 1.17 and 1.33 MeV equaling a total energy of 2.5 MeV combined, because the two occur essentially simultaneously. Additionally, associated with this decay is one beta particle emission. The PMT was enclosed in a light tight tent to reduce the dark count to minimal values. The temperature inside the enclosure was 22° C with 32% humidity. The source, described in Table 2, was visually centered directly on each crystal's surface, and the crystal was placed in front of the PMT's front aperture as shown in Figure 23.
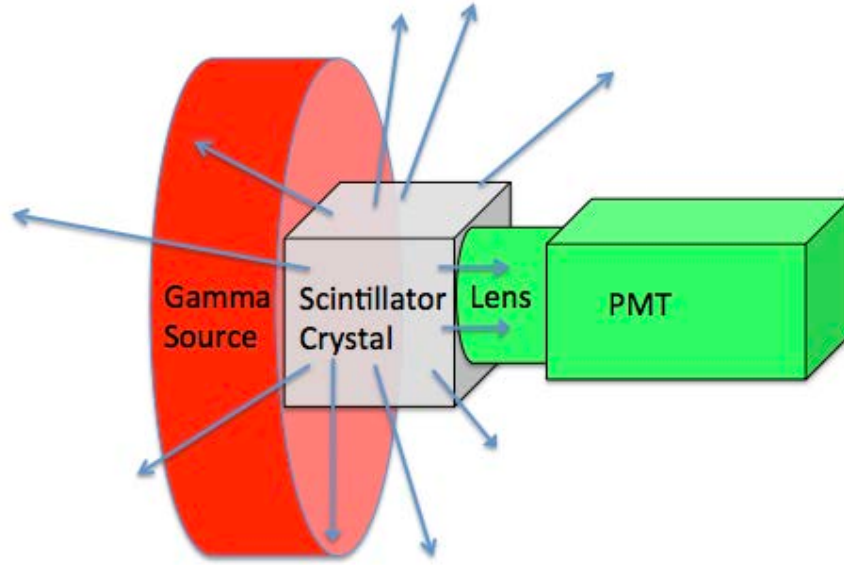
Figure 23.   Gamma radiation source and scintillator crystal position for diffuse source experiments.

Due to this placement, photon yield calculations (ph/MeV) were based on a diffuse source. The Hamamatsu software was set count photons every 100 m/s for 180 seconds. This experiment was performed to validate data from [17], but without testing the ZWO scintillator.

2.   Diffuse Source Gamma Excitation Results

The 1.17 and 1.33 MeV gamma radiations emitted from Co-60 occur essentially simultaneously so the incident energy upon the crystal is 2.5 MeV, which is beyond the 1 MeV energy range that fast neutrons are typically characterized [5]. In theory, this allowed the measurements to give an emulated response of inelastic scattering after the scintillator crystal produced gamma radiation from a fast neutron. Figure 24 shows the final results of diffuse source gamma induced radiation effects on all scintillators tested in Table 1. Table 3 shows the measured average scintillation yield for all scintillators. Light yield is calculated by using equation (1).

Table 3.   Co-60 Gamma source photon yield results for ISC crystals.

Crystal	Avg. Yield (ph/MeV)	Avg.Yield/V (L_R/m^3)
CWO	2873	357.2
BGO1	547.8	76.17
LGSO	260.1	82.23
BGO2	154.8	49.36
LuAG	89.45	28.66
PWO	29.74	6.25

Based on Z_{eff} /bulk characteristics alone, BGO1 and PWO, should have the highest scintillation yield. What is interesting is that CWO performed the best with an average of 2873 ph/MeV followed by BGO1 with 547.8 ph/MeV. PWO performed worse than BGO with 29.74 ph/MeV photon yield. As a reminder, in Table 1, each crystal was ranked according Z_{eff}/bulk density, which suggests PWO and BGO should have similar yields, and well above CWO and every other crystal for the most part. This was not found to be the case, which points to the fact that there are more factors involved in scintillation than just atomic number and density. If you isolate PWO and CWO on the table you can see that PWO has a higher density, but has the same cubic volume and a similar crystal structure [15]. A graphical representation with BGO, LGSO, PWO, and LuAG, plus the raw data from this experiment, is shown in Figure 24; CWO was excluded due to the dominant performance of the crystal when compared to the remaining crystal yield results. The yield data from column 1 in Table 3, obtained by equation (5) was divided by the volume of each crystal to provide ph/MeV*m^3, which allows a better comparison between the scintillator samples.
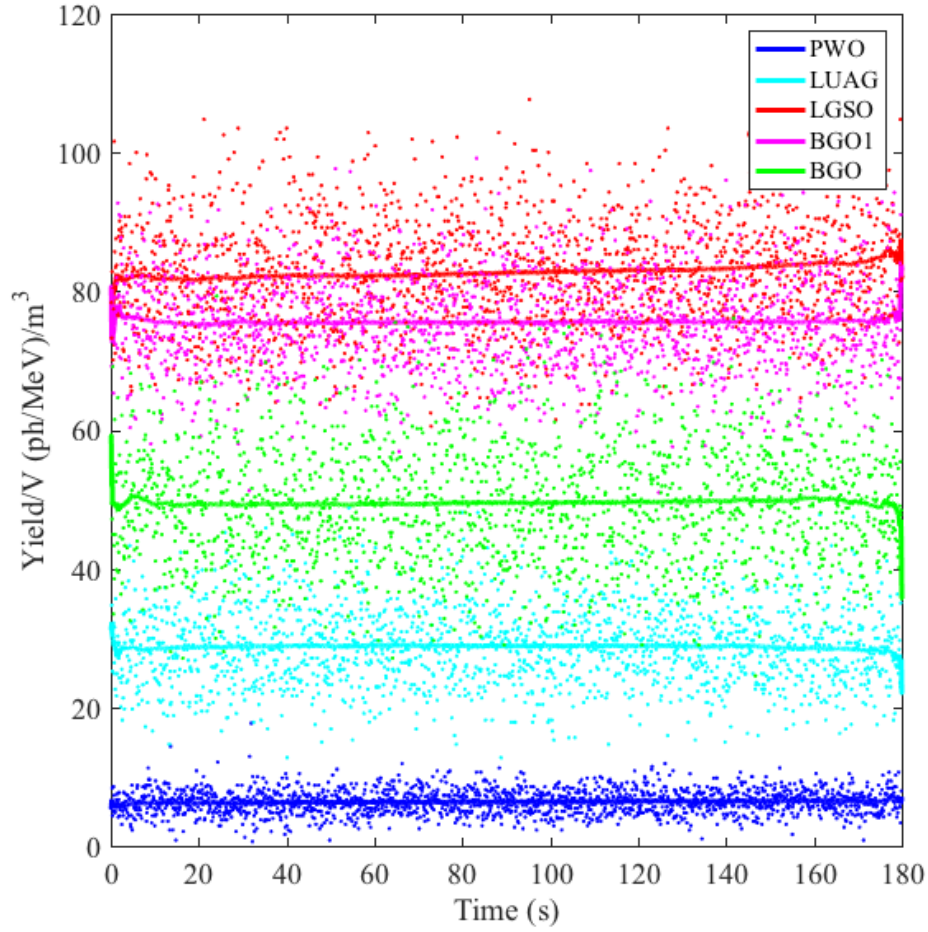
Figure 24.   Diffuse source Co-60 photon emission test with ISC crystals
excluding CWO and ZWO.

The results show that the crystals with a lower inelastic scattering cross section produce higher light yield than the scintillators with higher cross section. Additionally, with the PWO and BGO density numbers, both greater than CWO, and PWO and CWO having nearly the same volume, there should be no reason for CWO to outperform PWO by more than 9,700%. After more research into the properties of the crystals it was found that temperature dependence could play a significant factor in photon yield. According to Grinyov, BGO and PWO both increase their yield output as the temperature is decreased [15]. For BGO, this factor is increased almost by one order of magnitude as temperature

decreases to freezing (~0° C) levels [15]. The factor of temperature dependence is important here as it leads to the next experiment to test this hypothesis.

3.   Temperature Dependence

The same setup in the previous experiment was repeated, except that a couple of factors were changed to better understand why PWO and BGO were relatively low performers at room temperature. The temperature in the dark room was 24° C with 59% Humidity. BGO1 was placed in a refrigerator and cooled to a temperature of 4.9^o C, measured with a Fluke-87 multimeter with a thermocouple attached to the leads. After the crystal was removed from the freezer it was immediately tested. When the crystal was exposed to room temperature, its surface temperature increased on an average of 1.675^o C/min. The photon count temperature test was completed before BGO re-heated back to room temperature. Note that the temperature was always measured at the surface and not recorded internally. According to Grinyov, the light yield should increase by approximately 10–35%, depending upon the temperature of the crystal when measured [15].

As shown in Figure 25, there is a significant difference between the photon yield of BGO1 at room temperature versus near freezing. From the data there is approximately a 20.4 % difference in light output capture when the crystal is cooled, which corresponds consistently with the analysis of Grinyov [15]. It is important to note that condensation is a factor, but no steps were taken to avoid or reduce condensation on the surface of the crystal as it heated up. Also the raw data is graphed as well as the average signal to show the data dispersion, and the averages were calculated by using the data smoothing option in Matlab with 180 set as the span length, meaning, the graphed data average is a moving average of every 180 points.
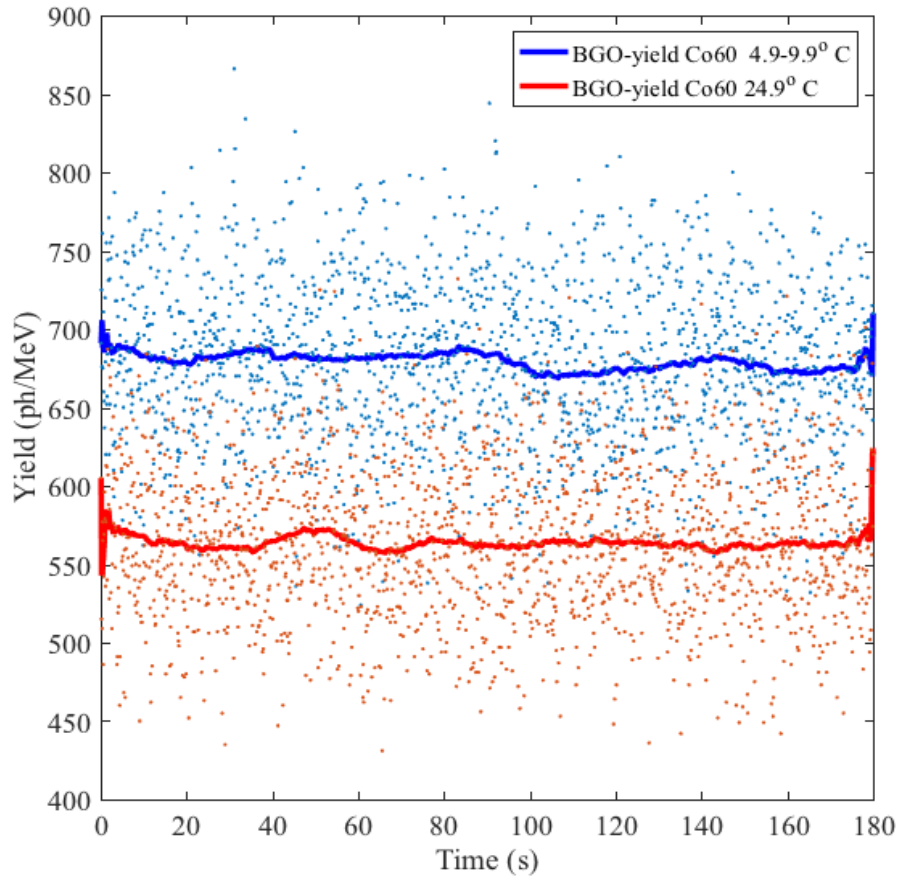
Figure 25.   BGO temperature comparison at 4.9-9.9 degrees Celsius and room temperature after Co-60 excitation.

The results shown in Figure 25 illustrate that the crystalline structure of PWO and BGO is metastable, meaning their structure varies with temperature and incident energy. As temperature decreases, less incoming energy is absorbed to transfer from one state to the next more preferred state [24]. Basically, thermal quenching occurs because of the lattice structure of PWO and BGO exhibit luminescence-quenching mechanisms that compete with the radiative relaxation of the excitation [16]. According to Klassen,

> when the electron structure of the crystal is excited locally either by optical photons or by ionizing radiation the interatomic electron bonds become more weak resulting in the decrease of elastic barriers. Due to this reason, the atomic structure can transfer to a more stable state. [26]

45

Although this explains some of the crystal's light yield problem associated with this test setup, the overall photon yield numbers are low compared to those of Lecoq, who measured a yield of 8000 ph/MeV for BGO [14]. The average of 548 ph/MeV is more than one order of magnitude lower than the experimental results from Lecoq [16]. One possible explanation is that most of the scintillation light is not read by the PMT as shown in Figure 23. Once the radiation excites the crystal to a state of light emission, and the light ultimately escapes on each crystal face, including the crystal face closest to the PMT, there are angular losses throughout the crystal on the sides not perpendicular to the PMT entrance plane (see Figure 23). Therefore, another experiment was performed in order to maximize the capture of the photonic response of the crystal by channeling the light that may be lost on the other crystal faces.

4.   Point Source Photonic Focus

In an attempt to maximize the capture of the photonic response of the scintillator, aluminum foil was wrapped around ZWO and the response was measured with Co-60's incident gamma radiation. The thickness of the foil around the crystal was .05 inches. However, the introduction of the aluminum foil appeared to reduce rather than increase the photon count, an observation that deserves additional investigation. One factor that could account for a portion of this observation is the hypothesis that the foil attenuated the contribution to photon output from the beta particles emanating from the Co-60 source. Therefore, the source was wrapped in aluminum foil and the crystal was tested with and without foil in response to a wrapped source. Additionally, the crystal was 15mm from the crystal so there is a reduction in photon response from the distance, as is discussed in the next experiment setup. After taking these factors into account, the results from the experiment, are shown in Figure 26.
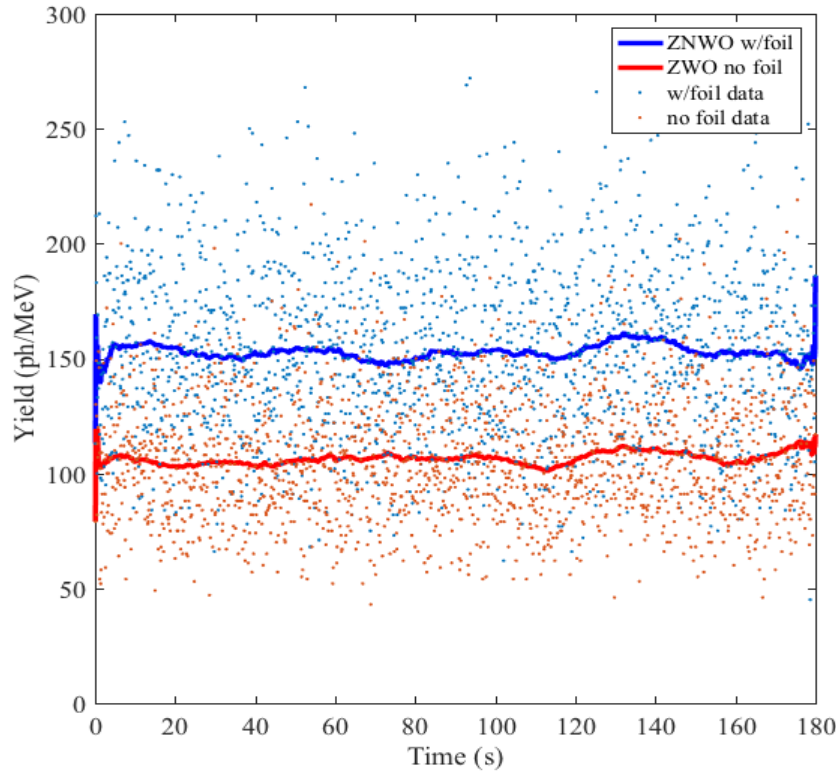
Figure 26.   ZWO at 15 mm using Co-60 source with and without foil wrapped
on all sides.

The results in Figure 26 show that the scintillation light increased significantly by focusing as much light as possible into the PMT aperture. The overall average measured photon yield captured, was 50% higher with foil than without foil. While this experiment does not explicitly analyze reabsorption or double emission, it does allow us to increase overall scintillation yield capture, if necessary, in a relatively rudimentary and cheap way. Additionally, according to Lecoq, "experimental light yield can be significantly lower due to traps and some e-h combinations that are not useful producers of light in complicated crystalline structures" [16]. Additionally, in [16], the light yield values were obtained from several other references with different experiment setups for each, which does not allow for a fair comparison of light yield obtained. Yet, this test was conducted as a point source experiment, unlike the previous diffuse source setup. Additionally, these scintillators will be used in detection devices in which the scintillator will not be directly

in contact with the source. Therefore, a better understanding of signal output as the distance of the source varies is necessary.

5. Point Source Gamma Excitation

Since scintillator radiation detection in the practical sense will generally be at some distance from the source, the next experiment was setup to vary the distance and measure the photon yield. To assist in the comparison of yield from previous measurements, the same Co-60 source described in Table 2 was positioned at distances of 10, 20, and 30 mm from the face of the crystal. Since CDWO performed the best at room temperature, it was the only crystal used. The results from this experiment are shown in Figure 27.

Figure 27.   Point source data for CDWO with Co-60 source varied at 10, 20, and 30 mm.

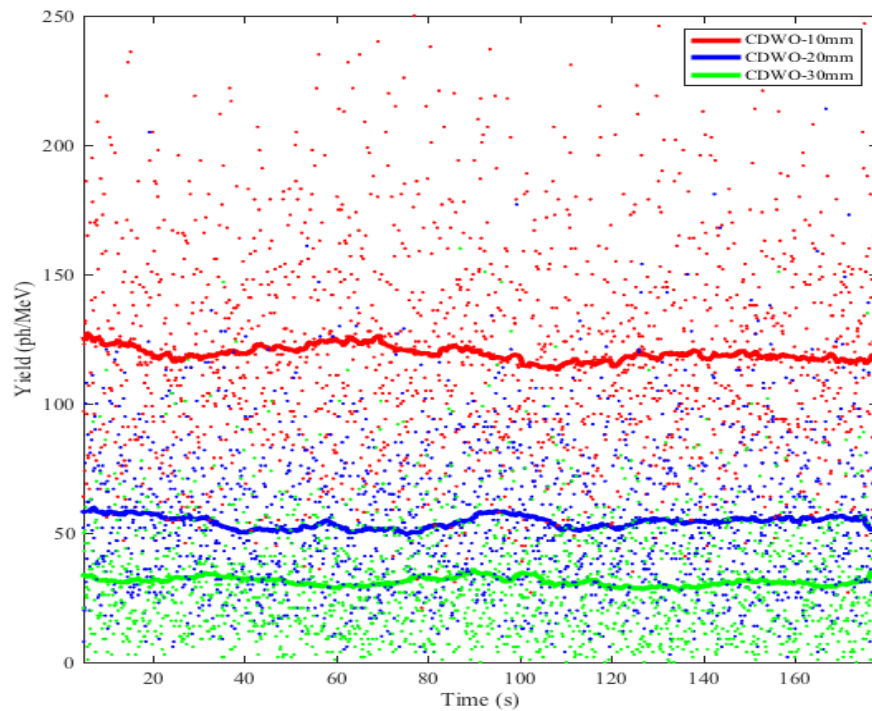As expected, the measured scintillator light yield decreased with distance as a function of source strength. What is good to note is that after 10 mm the average signal is less than 200 ph/MeV for a relatively high energy but at a relatively small practical distance. The fraction of energy deposited in the crystal from the source at 10, 20, and 30, mm equals 19.26, 7.96, and 3.54% of the total isotropic energy respectively, based on solid angle. Thus, at 20 mm the photon yield should be around 49.077 ph/MeV and at 30 mm the photon yield should be around 21.546 ph/MeV. The actual values were 54.28 ph/MeV and 31 ph/MeV for 20 mm and 30 mm respectively. At 20 mm there is an 11% difference between the measured value and the theoretical expectation, but at 30 mm there is a 44% difference and it is unknown as to why this occurred. More tests need to be done with distance to see if these results can be repeated. One limitation of this experiment setup is that it cannot differentiate wavelength without an abundant use of filters. To avoid this, the next experiments conducted, using the PCS, were to find the peak emission wavelength for each crystal.

B.   EMISSION WAVELENGTH-GAMMA INDUCED

The limitation of the previous experiments is that the setup does not allow you to obtain photon count per wavelength, therefore spectroscopy cannot be done reasonably. This may be acceptable for practical application if one has only one crystal, and is not concerned about multilayer crystals with different wavelength emissions per crystal. However, new advancements in scintillator detectors use spectral characteristics to understand response [27]. The PCS discussed in Chapter III was the best available and most accurate resource for wavelength measurement at the time. It was believed that the most responsive crystal should be used to ensure that the signal was received by the PCS, and LGSO was chosen as the first candidate.

1.   LGSO Peak Emission Diffuse Source

LGSO was chosen as the first scintillator to be characterized, due to the Cerium activated luminescence center which figured to provide a strong response. The lack of information found regarding LGSO's peak emission wavelength was also a factor in choosing LGSO for this test. The mount used for this setup was measured to be 12.02

mm thick which is added to the base of the test sample plate inherent with the JOEL 840 light tight chamber. The dark count was recorded with the LGSO crystal in the chamber without any incident radiation from 360–550 nm. The SR560 amplified the signal by 2×10^2, and the dark count was measured at 14.8 counts/s, with 200 runs at a .1-15 V threshold. After this recording, the same Co-60 source used previously in this study was used to simulate fast neutron energy scintillation. The source was placed directly under the crystal and aluminum foil was wrapped around the crystal and source with one face of the crystal free of foil underneath the parabolic mirror. The measurement was performed in the same manner as the dark count. The results are plotted in Figure 28, which point to several issues.
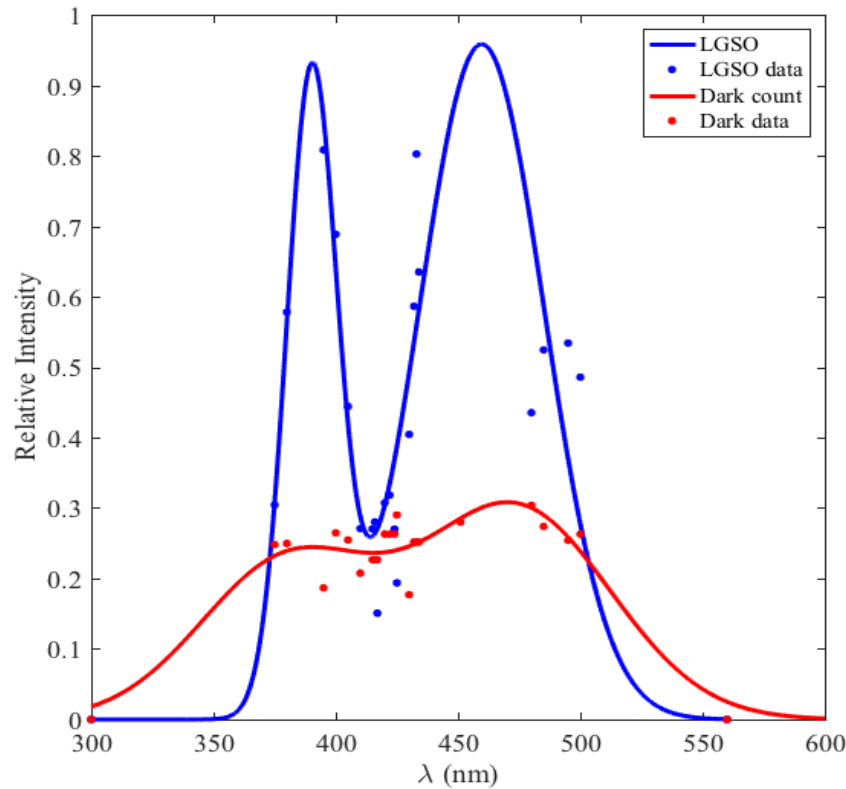

Figure 28.   LGSO peak emission tested with Co-60 source inside PCS.

Since the spectral response, especially the emission peaks, is more important in these tests than photon counts, the graph was normalized to allow easier comparison. The data

points are plotted as circular marks. The solid lines for the dark count and crystal response are fitted plots. These Gaussian fits are fitted using the data indicated by the circular marks with a Gaussian fit operator in Matlab. Matlab uses equation 11 to fit the data [28].

$$y = \sum_{i=1}^{n} a_i e^{\left[-\left(\frac{x-b_i}{c_i}\right)^2\right]} \tag{11}$$

Where n is the number of peaks to fit, a_i is the amplitude, c_i is determined by the peak width, b is the centroid [28].

First, according to Figure 28, LGSO has two-peak emission wavelengths at 395 nm and 460 nm. Secondly, this seems to correspond to the natural emission wavelength of the crystal with no source (see dark count). One possible explanation described is that, in the initial experiment, the LGSO crystal was exposed to light in order to set up dark count measurements and stimulated emission measurements. This may have stimulated the crystal from the light exposure in the room and contributed to the dark count. However, it is unknown why LGSO has two peak emissions rather than one. This experiment will need to be repeated in order to validate this measurement. Additionally, according to Lecoq and Rusieki, the peak wavelength should be around 416–430 nm [16], [17]. It was initially assumed that we are measuring two distinct emissions, one from the Cerium activation and another from the GSO portion of the crystal, but according to Grinyov, GSO peaks at 430nm and LSO peaks at 420 nm [15]. One possible cause for this aberration, would be the background light entering the chamber, the way the experiment was conducted, or lack of data points. Since no care was taken to shield the crystal while setting up the experiment and less care was taken to reduce the dark count form light outside the chamber this test result was discarded. Additionally, this test was completed before the posi-drive belt failed, as described in Chapter III and is not directly repeatable.

2. LGSO Peak Emission Retest

a. *Method*

In order to understand LGSO's performance in the previous experiment, another experiment using LGSO was conducted. In this experiment, the radiation source was placed directly beneath the crystal, visually centered underneath the parabolic mirror, and then centered for maximum response. A 6.3 mm mount was used and the X, Y, and Z settings on the PCS location knob indicators were 4.7, 4.4, and 8 mm respectively. The power supplied was 2000 V and the oscilloscope was set to 10 m/s set per division. The wavelength range that was to be scanned was set from 330 to 550 nm at 5 nm increments in order to find the peaks from the previous experiment. The PMT was cooled at -30° C for 24 hours in order to get maximum signal with little or no noise. The same Co-60 source, used repeatedly throughout this research, was used again in this first re-test. After Co-60 was used, Cesium-137 (Cs-137) and Sodium-22 (Na-22) were used in the second and third iterations to see if the reason for the two peak emissions depended upon incident gamma quanta. Tables 4 and 5 describe the Cs-137 and Na-22 sources used.

Table 4.   Cesium-137 Gamma source.

	Cs-137
Activity	1 uCi
Half-life (yrs.)	30.3
Energy (MeV)	.662
Manufacture Date	August 2006
Thickness	3.03 mm
Diameter	6.77 mm

The decay of Cesium is annotated as equation (12) [5].

$$^{137}_{55}Cs \rightarrow \, ^{137}_{56}Ba + \, ^{0}_{-1}e + \gamma \tag{12}$$

52

In equation (12) Cesium decays to Barium-137 (Ba-137) by emitting a Gamma of .662 MeV and a beta particle. The Na-22 source is described briefly in Table 5 and equation (13).

Table 5.   Sodium-22 Gamma source.

	Na-22
Activity	1 uCi
Half-life (yrs.)	2.6
Energy (MeV)	1.275
Manufacture Date	September 2006
Thickness	3.03 mm
Diameter	6.77 mm

In equation 13, the decay of Na-22 differs from that of Co-60 and Cs-137 in that it emits a positron instead of an electron and emits a gamma ray before becoming Neon-22 [5].

$$^{22}_{11}Na \rightarrow\, ^{22}_{10}Ne +\, ^{0}_{+1}e + \gamma \tag{13}$$

b.   LGSO Peak Emission Test Co-60

Note from the previous measurement of LGSO spectral response, the peak emissions were found to be around 395 and 460 nm. These values differ from previously published results, therefore the experiment was repeated four times and the results were averaged and graphed as shown in Figure 29.
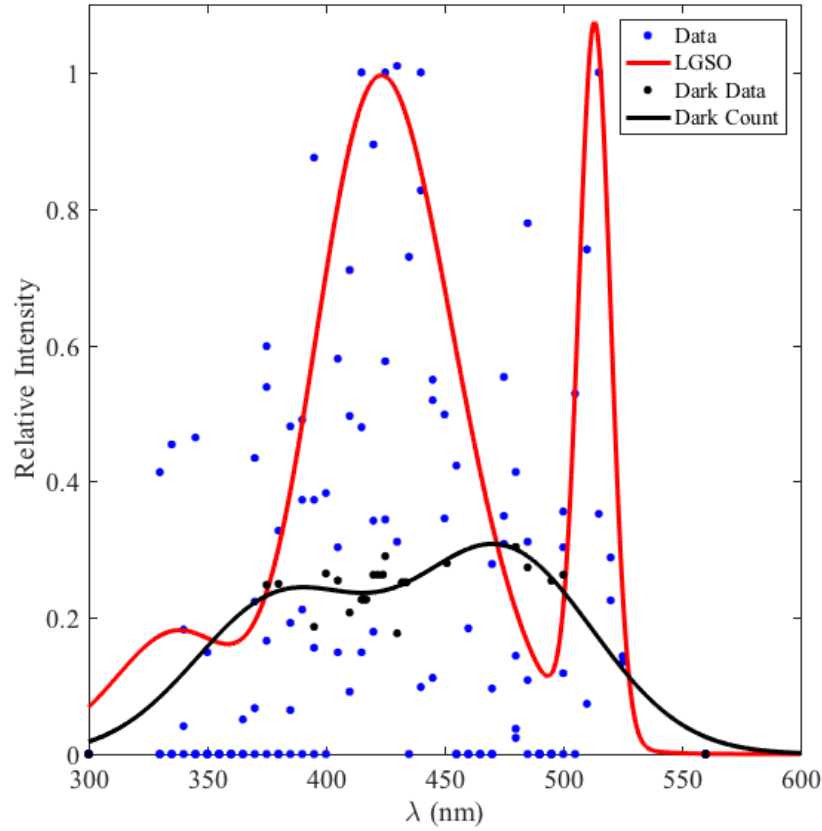
Figure 29.   LGSO peak emission re-test with Co-60 to determine the peak
emission of LGSO.

In Figure 29, the entire data set from the four tests was fitted using equation (11) in Matlab. What is interesting to note is that there is a definite peak emission that is repeatable at 423 nm, which corresponds to the published 415–430 nm peak emission wavelengths for the LGSO crystal [16], [17]. Additionally, in accordance with the previous LGSO peak emission test, there is a second emission peak at 512 nm, which somewhat corroborates the initial test, however the intensity is far less than the peak emission that occurs at 423 nm. Note, in this experiment, unlike the previous one, after dark count was taken, the crystal and the source were placed on the mount in the dark. Regardless, the new finding in this experiment was the second emission peak at 515 nm. Two of the four tests produced a second peak at this wavelength. It was assumed the 423 nm is due to Cerium concentration and it was unknown at this time why the second peak

54

occurred. In order to repeat this, a third emission test was performed to confirm that LGSO indeed has two emission peaks.

c. *LGSO Peak Emission Test#3 Co-60*

In order to find out whether or not LGSO truly emits light at several wavelengths, a third experiment was performed, and this time more care was to be taken not to expose LGSO to ambient light before testing. Additionally, the crystal was placed at a location in which maximum photon response could be achieved by adjusting the crystal location until there was maximum photon response around 420 nm. Additionally, the crystal was placed in the chamber 14 hours before testing to reduce dark count measurements and increase the signal to noise ratio in the experiment. The location of the crystal and Co-60 source was at the indicated values of X = 17.15, Y=11.2, and Z=8.0, with a mount approximately 6.33 mm in height. The settings on the oscilloscope and the SR560, were the same as the previous experiment. However, the threshold for count was set from 0.01-15 V, with a wavelength sweep of 330 nm to 530 nm. The results from this experiment are shown in Figure 30.
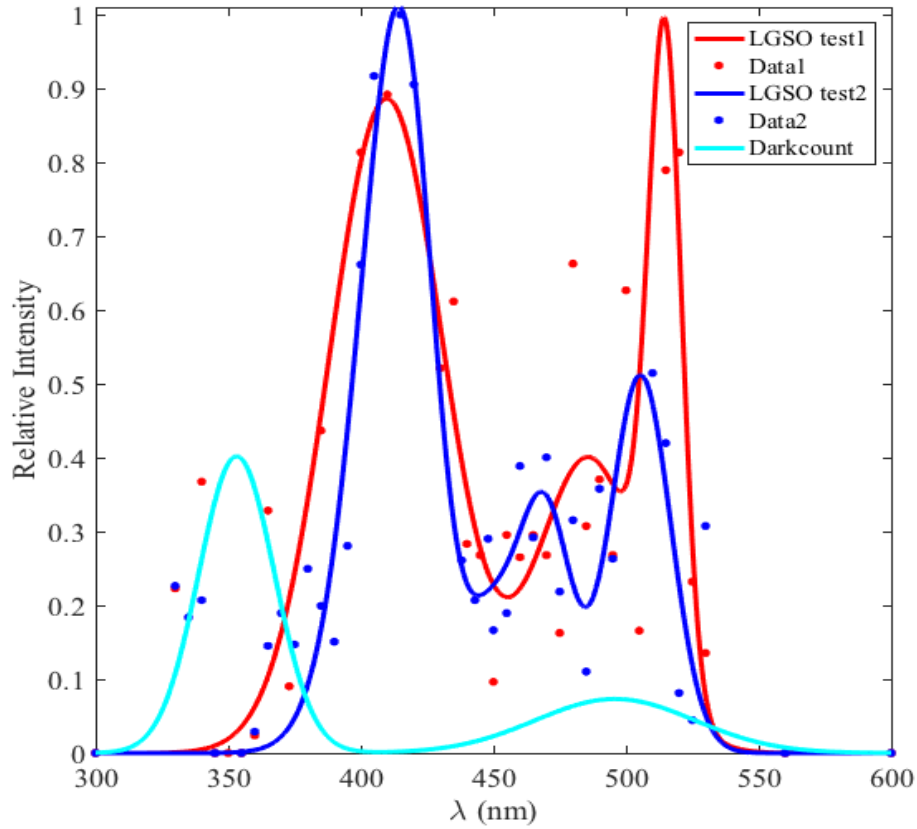
Figure 30.   LGSO dual peak emission confirmation using Co-60.

As shown in Figure 30, there is indeed a dual peak emission performance of LGSO. Albeit, the relative intensity of the second peak is half the intensity of the first test, this second emission was found again around the same wavelength. Although the main peak emission from the two tests are 410 nm for test 1 and 415 nm for test two, the second peak measured was at 505 and 515nm in test 1, corresponding to the previous test results of 505 and 512 nm in this test. This suggests that the range of the second peak is 502–515 nm. According to Kurata, the causes of these two peaks are due to two distinct luminescence sites that the Cerium dopants occupy [29]. By this is meant that the Cerium dopants, depending on location, emit at two separate wavelengths [29]. The data in Figure 30 is in strong support of Kurata's findings. However in order to eliminate a hypothesis that energy level had something to do with the two peaks, Cs-137 and Na-22 were used to excite the crystal to verify if peak emission was not dependent upon incident energy.

d. LGSO Peak Emission Test with Cs-137

The same setup from the previous experiment was performed with Cs-137. The only variable changed was the incident gamma quanta. It is expected that the peaks will not change depending upon activation energy deposited. In Figure 31 the results of two sweeps from 300 nm to 600 nm are shown.
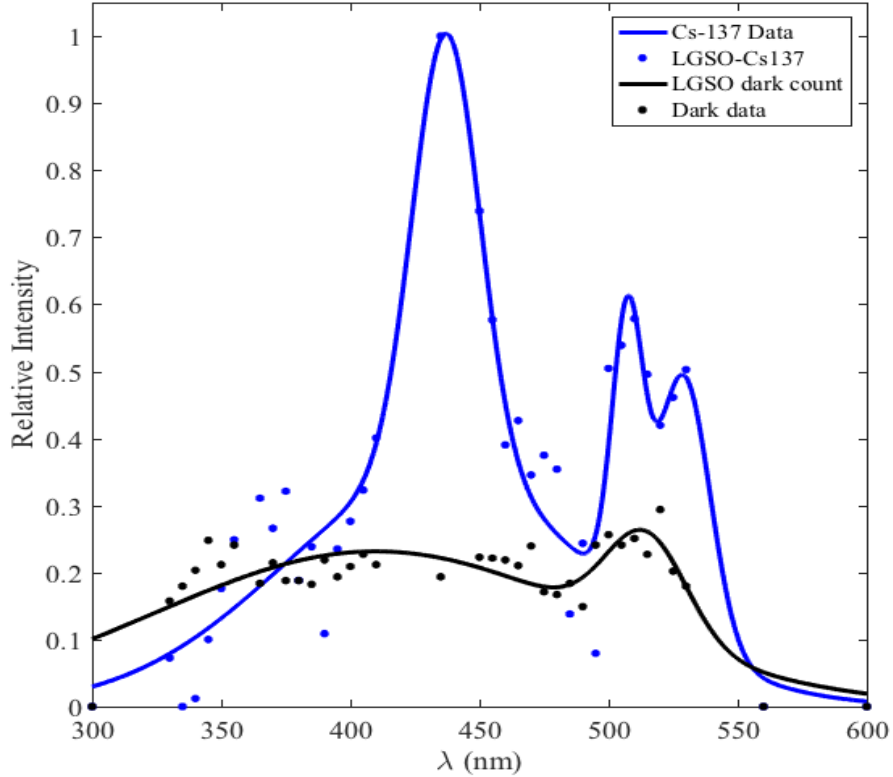
Figure 31.   LGSO dual peak emission confirmation with Cs-137.

As shown in Figure 31, there are two peaks, albeit one is 60% less than the major peak. Remember in the previous experiments the second peak was sometimes less than the major peak if it manifested. Note that the major peak is at 432 nm which is in good agreement with that of [16], [17]. The error could be caused by a variety of factors including the small data set, error in calibration, or sample size. However, in order to establish a clear primary peak of emission for LGSO a different energy source, Na-22, was chosen for the next test immediately following the test shown in Figure 31.

e. LGSO Peak Emission Test with Na-22

In order to come to a final conclusion on peak emission for LGSO under varying energies, the same crystal was tested with Na-22, to confirm the primary emission peak wavelength. Note, no settings where changed or manipulated from the previous Cs-137 test to get the data shown in Figure 32 in order to reduce human error in the measurement.
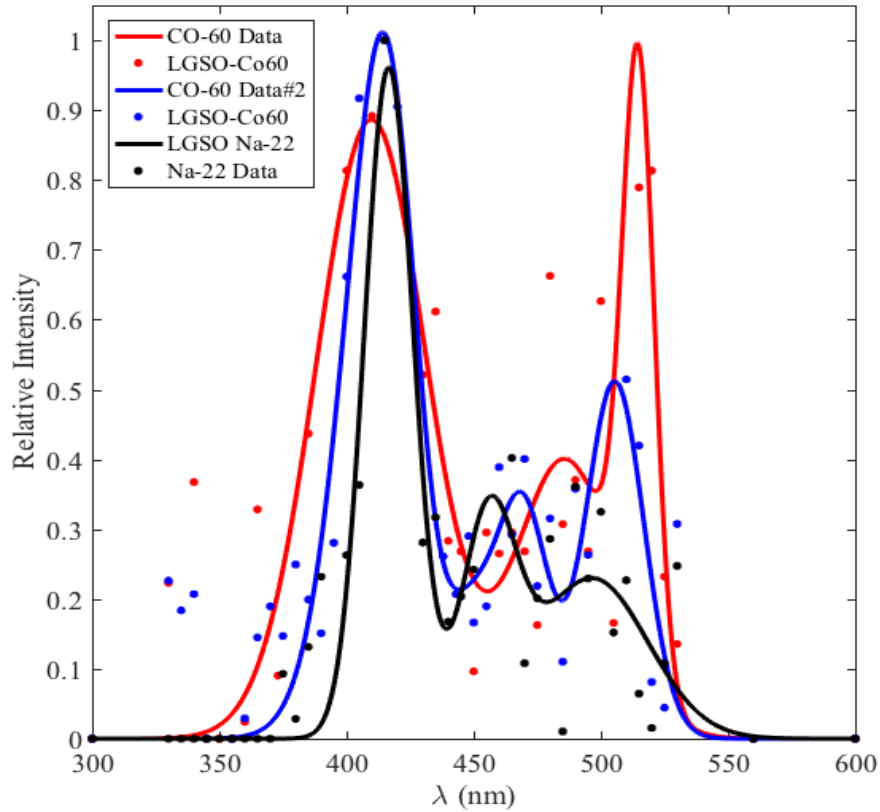
Figure 32.   LGSO primary emission peak confirmation using Na-22 and Co-60.

Please note that the dark counts are not plotted here because these tests were completed on different days with different dark counts. As shown in Figure 32, the primary peak corresponds to approximately 415nm. The data from Na-22 was overlaid with the previous Co-60 data to show similarity in response. The second peak is not as prominent in this figure. Six out of the 8 tests resulted in a primary emission peak of 410–416nm which is consistent with what has been previously published [16], [17]. Therefore,

although the peak emission can range from 415–430 nm, the most likely emission will be around 415nm consistently. The next question is whether or not LuAG:Ce has a peak emission around 415 due to the Cerium dopants in the crystal and does it have a second peak as well?

3. LuAG Peak Emission Test

a. *Method*

Since LGSO has a peculiar dual peak response when subjected to gamma radiation, it would stand to reason that LuAG may have a similar performance based on the fact that it too has Cerium content. According to Lecoq, the peak emission wavelength of LuAG is 520 nm, while for this particular crystal Rusieki found a peak emission at 630 nm [16], [17]. Based off these two published findings, two peak emissions for this crystal were expected. In order to verify this, LuAG was placed in the PCS chamber for dark adaptation for 14 hours. The PMT was cooled to maximum cooling (approximately -30° C) with a water flow rate of .68 Gal/min for over 24 hours. The remaining setup is a repetition of the previous LGSO tests.

b. *LuAG Results from Co-60 and Cs-137*

As shown in Figure 33, there are two distinct, but similar peaks at 432 and 630 nm, one of which corresponds to the findings of Ruseiki at 632 nm [17].
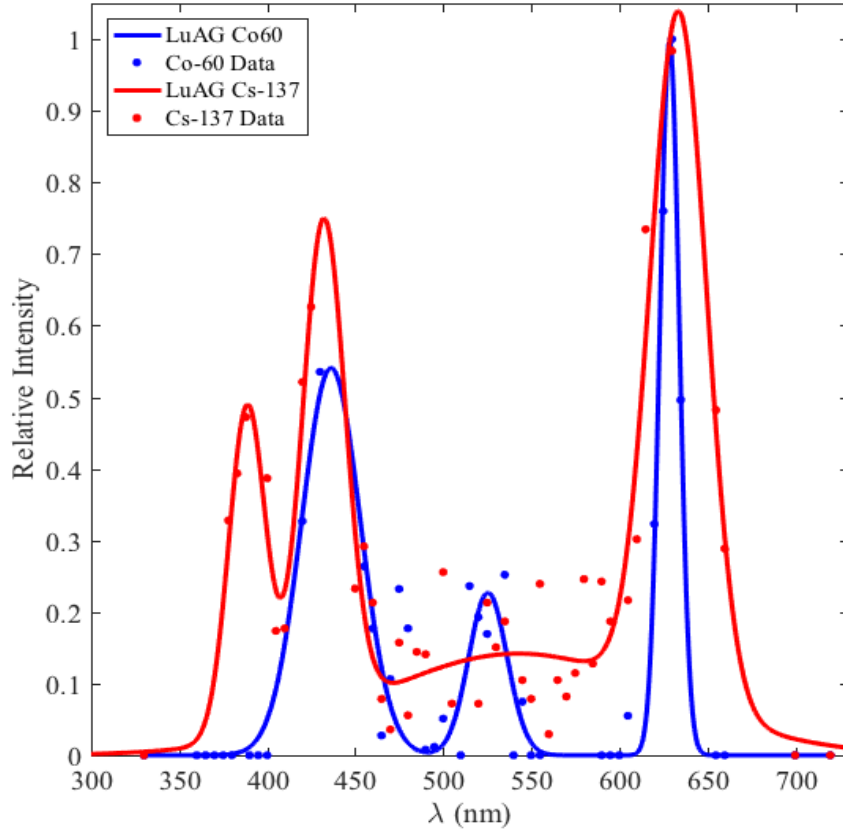
Figure 33.   LuAG dual peak emission phenomena using Co-60 and Cs-137.

This red shift from Lecoq measurement of 520 to 630 nm is due to the Cerium concentration in the crystal and is explained in detail by Ruseiki [17]. The 432 nm peak is close to the 415 nm peak finding in LGSO, and it is believed that this occurrence is similar to the two luminescent center finding of LGSO [29]. Therefore, to some degree this dual peak has some validity within the range of 415–432 nm. What is interesting is that this peak is roughly 20 nm away from LGSO's primary peak. To ensure that it is not a PCS error a third crystal without Cerium dopants was chosen were the estimated peak emission is well beyond the 415–438 nm range.

4. BGO Peak Emission Test

a. *Method*

BGO was chosen as the next crystal for testing because of the similarities to LuAG and LGSO in fabrication size and shape, and the peak emission range of 505–518 nm [16], [17]. The crystal was placed in the PCS chamber overnight for approximately 14 hours and tested for dark photon counts. The wavelength testing range was 380–580 nm with at 5 nm increments for 10 s. The crystal was centered for maximum response near the focal point at knob settings of X=17.6, Y = 16.4 and Z = 15mm from the mirror. The remaining test parameters are the same as in previous experiments.

b. *Results*

According to Figure 34, the peak emission response wavelength for BGO using Co-60 is equal to 508.8, which is in good agreement with what Lecoq found at 505nm [16]. The purpose of this test was twofold, 1) Confirm that the 415–438nm response is indicative to only LuAg and LGSO from the heavy organic crystals tested; 2) Confirm that there is not an error in calibration or experiment setup that could contribute to a systemic approximation of a 415–438 nm second peak. Both purposes have been fulfilled.
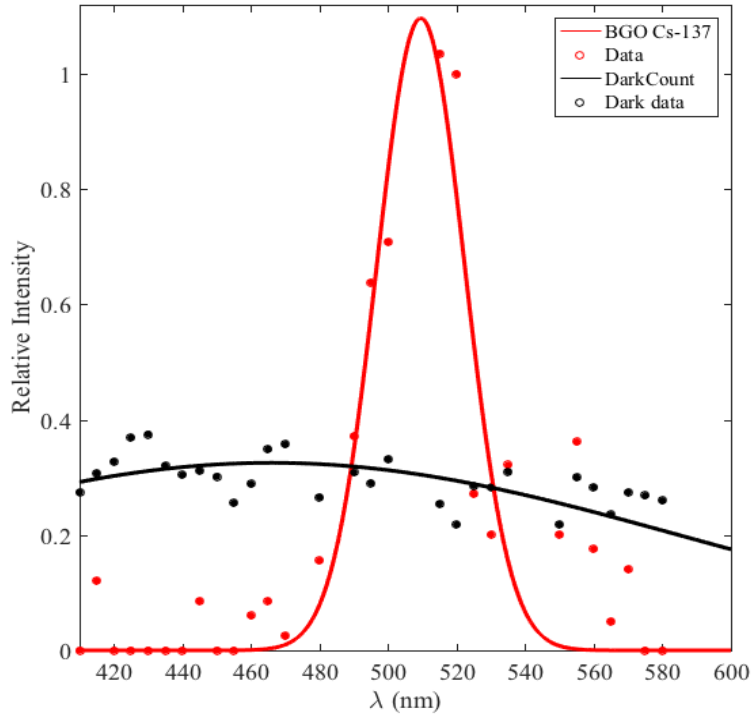
Figure 34.   BGO emission peak performance with Co-60.

Below 480 nm there is no significant response. From this data there seems to be no need to conduct more tests on this crystal with different energies since this single peak is evident and there does not seem to be any dual peak response. The remaining crystals were tested for peak emission to validate the experiment setup and further characterize these heavy oxide scintillator crystals for use in further study.

5.   PWO, CWO, and ZWO Peak Emission Tests

a.   *Method*

The three Tungstate crystals were tested for peak emission to complete the peak emission characterization of the crystals given to NPS listed in Table 1. CWO and ZWO were placed in the PCS chamber overnight for approximately 14 hours and tested for dark photon counts, but PWO was not because the dimensions of the crystal are different than those of CWO and ZWO requiring re-alignment with the focal point. The wavelength testing range was 350–550 nm with at 5 nm increments for 10 s for PWO and 400-650

nm for CWO and ZWO. Each crystal was centered for maximum response near the focal point. The remaining test parameters are the same from previous experiments.

b.   *Results*

According to Figure 35, the peak emission response wavelength found for PWO, ZWO, and CWO using Co-60 are equal to 439, 518, and 496 nm respectively. CWO is in good agreement with what Lecoq found at 495 nm [16]. While PWO is in good agreement with what Ruseiki found at 433 nm [17].
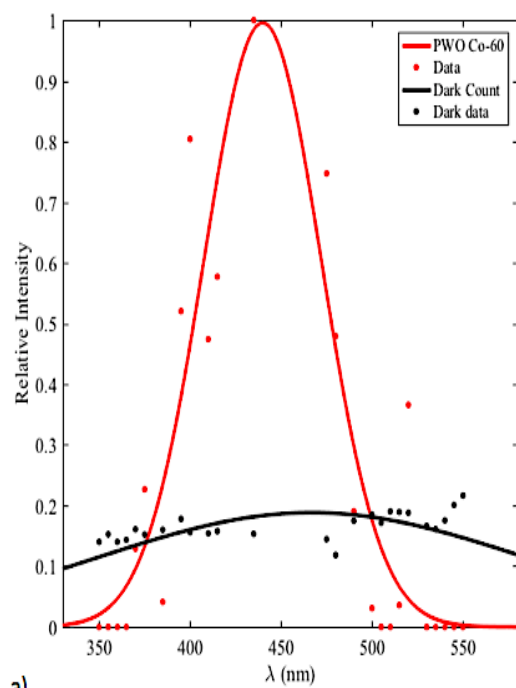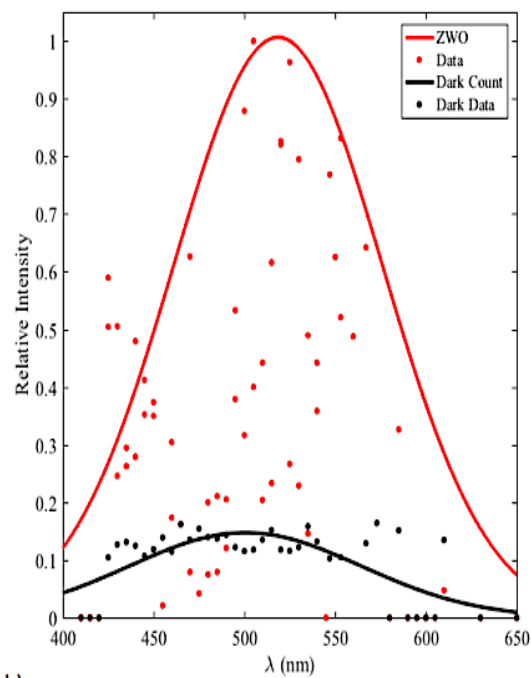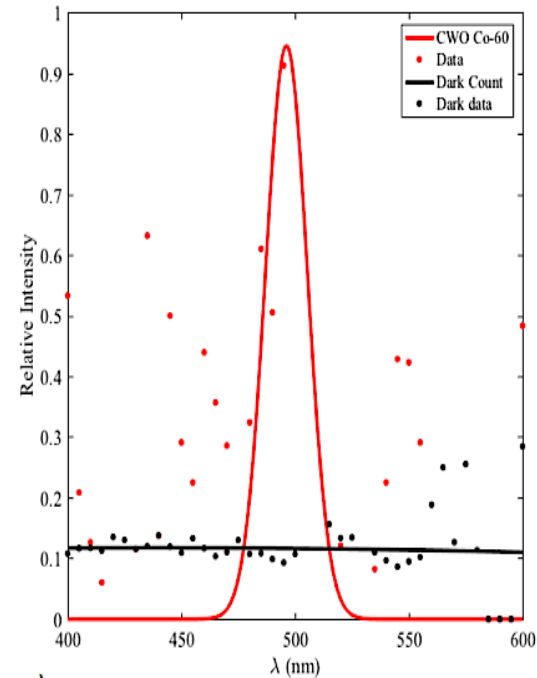
Figure 35.   Peak emission wavelength for PWO, ZWO, and CWO with Co-60 incident energy. a) PWO b) ZWO c) CWO.

While the result for ZWO is approximately 14 nm from what Ruseiki found at 504 nm [17]. This is partially due to the error in the fit, as there is a peak emission data point found at 505 nm. This test was the final test in peak emission characterization of the scintillator crystals in this study. The next step is to use the LTCFP to understand the effects of scintillator response to fast neutrons where knowledge of these peak emissions will become useful.

C.   FAST NEUTRON SCINTILLATOR RESPONSE

1.   West Point/USMA Neutron Test

In order to gain understanding of the scintillators response to fast neutron particles, a trip was planned to United States Military Academy (USMA) in West Point, New York and the United States Naval Academy (USNA) in Annapolis, Maryland, where neutron sources are available. Unfortunately, the PCS is not portable therefore the LTCFP was used first at West Point, New York with the USMA's Neutron Howitzer. The Pu-Be Howitzer characteristics are displayed in Table 6. For each setup the crystal was placed on a stand 15 mm from a New Focus 2151 photoreceiver as shown in Figure 36.
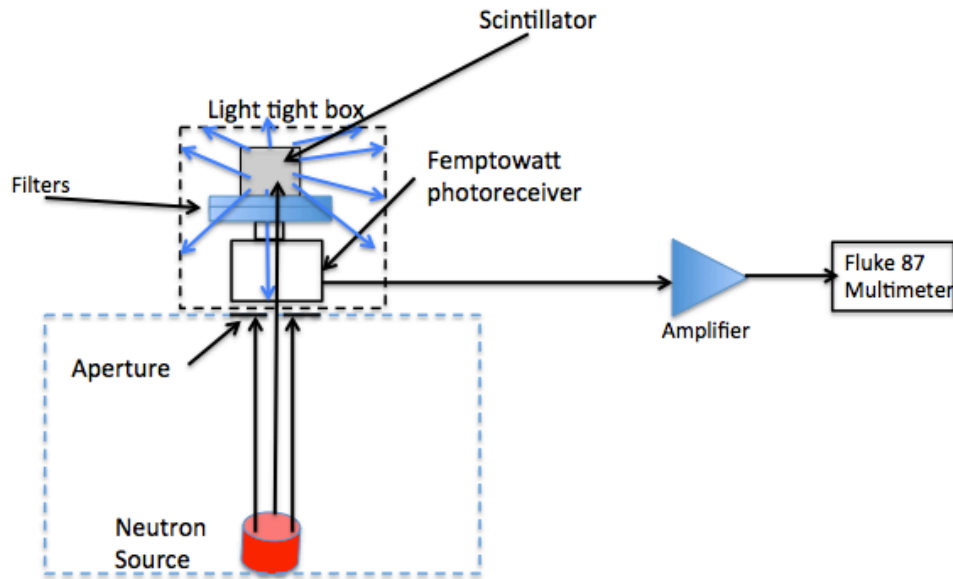
Figure 36.   Neutron Howitzer and LTCFP experiment setup.

One FSR-GG400 400 nm and one 10SWF-550 newport filter were placed in between the receiver and the crystal being tested. The filters were placed between the crystal and the receiver in order to get an accurate measurement of the total energy captured by the photoreceiver. With that measurement, plotting the spectral response to neutrons could be easily achieved with the experiment results from the PCS. The 10SWF-550 filter reduces light output above 550 nm and the FSR-GG440 cuts all frequencies below 400 nm. The spectral responses of both filters are shown in Figure 38.

Table 6.   Pu-Be Neutron source. Adapted from [30], [5].

	Pu-Be
Activity	1e6 uCi
Half-life (yrs.)	24100
Energy (MeV)	4.5 MeV
Manufacture Date	February 1961
Quantity	5

The isotopic reaction from this process is described in equation 13 [29].

$$_2^4He + _4^9Be \rightarrow _6^{12}C + _0^1n \qquad (14)$$

The production of neutrons from the Pu-Be source takes place in a two-step process. In the first step, Pu-239 decays by releasing an alpha (He-4) particle. The alpha particle then interacts with Beryllium in accordance with equation 14 to produce neutrons. The PCS was placed directly on top of the source approximately 365 mm on top of the howitzer instead of directly in line of the normal neutron beam outlet. The radiation dose measured on top of the box was 2.6 mrem/hour for neutrons and 3.8 mrem/hour for gamma radiation. The photon signals from the scintillators were filtered to allow wavelengths from 400–550 nm before being measured by the femtowatt photoreceiver. The signal from the femtowatt photoreceiver was amplified with the SR560 (gain=20). The signal output from the SR560 was averaged using a Fluke 87 multi-meter and the data was taken at room temperature of 24° C. The results of this experiment are annotated in Figure 37.
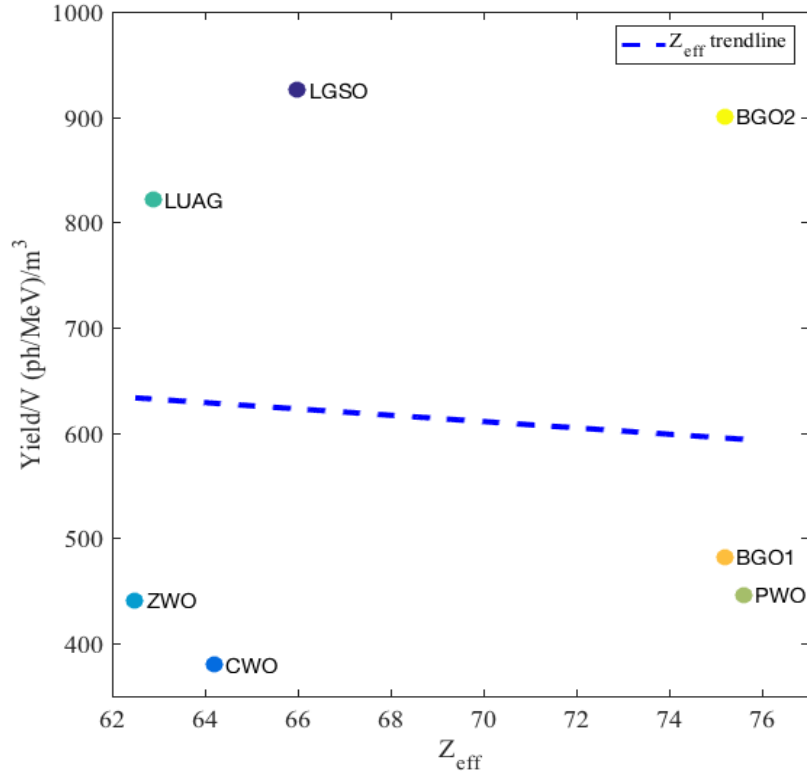
Figure 37.   Neutron howitzer results using the LTCFP graphed using Z_{eff} and dividing yield by crystal volume.

The yield is calculated by taking the voltage reading from the LTCFP and using equation (7) to calculate the results in photons/s and converting that to yield using equation (5) and equation (8). Then the values were divided by the volumes of each respective crystal in Table 1. From the results in Figure 37, it is important to mention that LGSO had aluminum foil wrapped around it, increasing the amount of light capture by the detector because there was some doubt that the signal may have been strong enough for the receiver to measure, as described in Chapter III. Additionally, the crystals were not shielded from gamma radiation, therefore this data is in response to both gamma and fast neutron radiation. Figure 37 shows that LGSO produced the most amount of light, corresponding to the high light output of LGSO in the gamma ray experiments completed in this study. Of consequence, BGO1 has the largest surface area of all of the candidates, meaning the physical cross section for absorption is much higher than the remaining crystals, yet had one of the lowest light yield performances per unit volume. PWO

provided one of the lowest yields/volume, but this may be because of thermal quenching explained in the gamma ray temperature experiments. However BGO2, which is also temperature dependent performed slightly below LGSO in light yield and it is unknown why this occurred and more study with fast neutrons is necessary. The Z_{eff} trendline was created by using the polynomial fit parameter in Matlab, which uses equation (15) to create the trend line [31]:

$$y = \sum_{i=1}^{n+1} p_i x^{n+1+i} \qquad (15)$$

Where n+1 is the order of the polynomial, n is the degree of the polynomial which can range from 1 to 9 [31]. In simpler terms, the trend line is a linear fit of the data from this experiment. From this trend line, note that the crystal's response to the source does not scale with Z_{eff}. This corroborates the hypothesis that there are a variety of factors that produce light yield in the crystals tested. Another important point from this experiment is the filter choice, as the 550 nm filter cuts off a considerable amount of LuAG's total spectral output, if the previous experiments data on LuAG's spectral output is correct. This would mean that LuAG's performance in this experiment is better than what is shown in Figure 37. In order to illustrate this, the spectral responses to gamma radiation were overlaid with the light filters used in this experiment and shown in Figure 38, where the shaded region indicates what was measured.
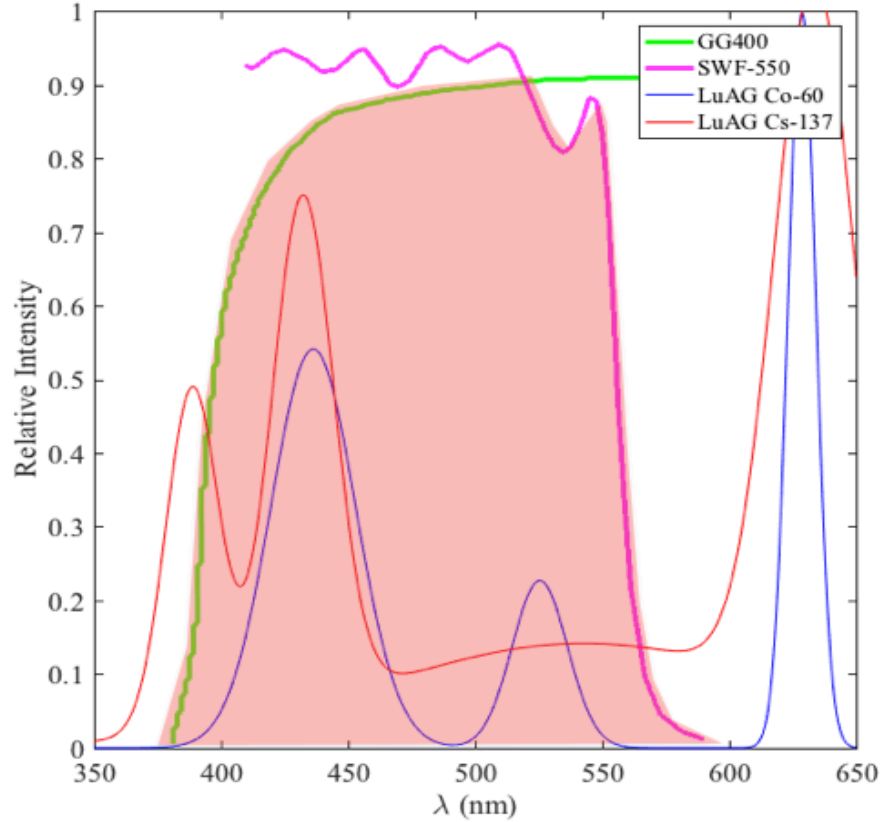
Figure 38. LuAG Co-60 dual peak emission data overlaid with filters used in fast neutron experiments.

As shown in Figure 38, if the data from the previous experiment regarding LuAG is a correct indication of the spectral output of LuAG, one peak emission point could have been cut using the 500 nm filter (SWF-550), reducing total spectral output considerably. The next step will be to conduct more spectroscopy analysis with neutron excitation to fully understand and characterize neutron response.

2.   USNA Neutron Test

The LTCFP apparatus did not change between WestPoint and Annapolis, but the energy output and configuration of the test apparatus was completely different. The USNA neutron source used was the thermo-electron deuterium-tritium (D-T) accelerator, which produces neutrons at a rate of $3x10^{10}$ n/s [31]. The circular 1 in. diameter disc produces a neutron beam, that spreads out isotropically. A 75' cord was attached to the

femtowatt photoreceiver to increase distance and reduce exposure device from source. Figure 39 shows a schematic diagram of the experimental setup.
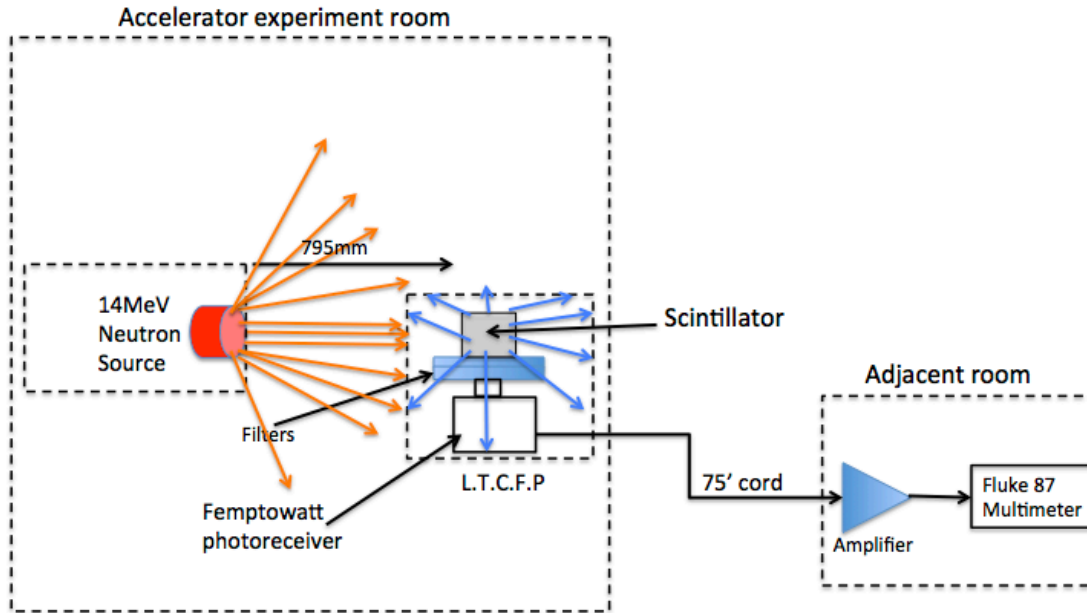
Figure 39.   D-T Neutron source experiment setup with LTCFP.

The equation for the D-T reaction is annotated in equation (14) [5].

$$^{2}_{1}H + ^{3}_{1}H \rightarrow ^{4}_{2}He + ^{1}_{0}n \qquad (15)$$

Figure 39 shows the initial D-T Neutron source setup. The energy of the neutron beam is a constant 14 MeV, and the signal measured by the LTCFP was amplified SR560 (gain =20) and filtered to allow readings from 30–1000 Hz. The crystals were placed approximately 790 mm away from the isotropic source. The data was taken at room temperature of 24° C. In Figure 40, the results shown are about what is expected and almost an exact repetition of the West Point test results with an increase in magnitude.
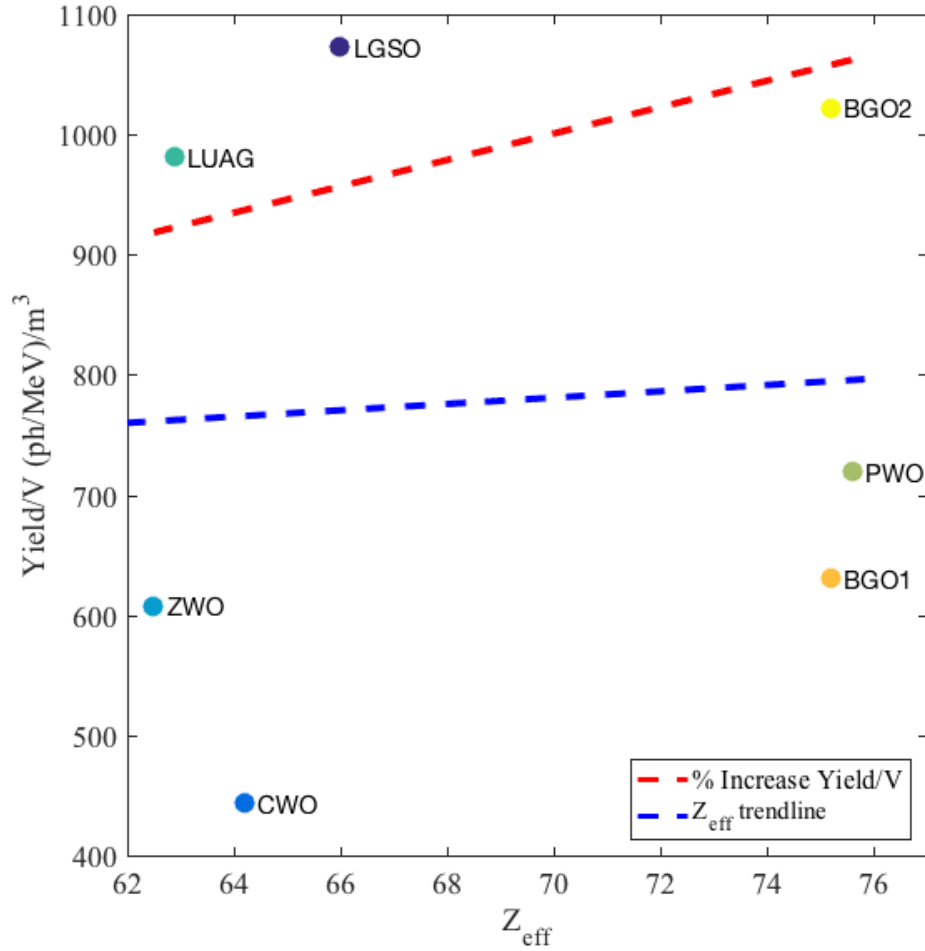
Figure 40.   D-T neutron source results with Z_{eff} trend line and % increase in light yield when compared to West Point test.

Here PWO performed better than the West Point test, despite the ambient temperature of the experiment setup. While BGO2 exhibited the second best light yield at this energy level at room temperature. If the L.T.C.F.P. had been cooled the results could be even more effective. Nevertheless, Z_{eff} ranking seem to scale with response, which is dissimilar to the West Point experiment. The main reason for this is the increased performance of PWO at this energy level. Additionally, for the PuBe source, neutron energy is significantly lower than for the D-T source; at higher neutron energy, the importance of inelastic scattering is greater, and this could contribute to a more positive slope. The red dashed line is the increase in light yield in percent when compared to the West Point test. This trend line was calculated by multiplying the percent difference

between the two tests by the D-T test. This red trend line tends to corroborate the hypothesis that the cross section for inelastic scattering is more important at higher energy, but it is unknown as to why this occurred and needs further study. The surface area for BGO2, LuAG, and LGSO are comparatively the same and the difference between the light yield is less than 6% between BGO2, LuAG, and LGO. Yet both Cerium doped crystals performed well. This may be due to the dopants in LGSO and LuAG, as in this experiment LGSO was not wrapped in aluminum foil to get maximum photon output because the lab technicians informed us that the aluminum foil would set off alarms within the D-T accelerator chamber. If BGO2 had been cooled for this experiment, the expectation is that it would be the best candidate from these crystals for future work, but the size would have to be reduced to that of the other crystals given, for proper classification and analysis. Here, just as in the West Point experiment, CWO and ZWO seem to not be the best candidates for fast neutron experiments in comparison to the other heavy oxide scintillators, but their response to gamma radiation is significantly higher than the other crystals.

This experiment was the final one completed and is considered the final step in this effort to characterize the scintillation of heavy oxide inorganic scintillators intended for fast neutron detection. Some of the insights obtained during this effort will add to the current knowledge base of scintillator crystals and their response. The last chapter in this thesis draws upon these experiment results and offers some thoughts about future experiments and analysis.

THIS PAGE INTENTIONALLY LEFT BLANK

V. CONCLUSION

A. SUMMARY

The preventative methods to avert a catastrophic nuclear event on American soil are limited, to some degree, by detection methods currently in use. Scintillators can be used to increase the efficiency and reduce the cost of current detectors because of their reaction characteristics when exposed to radiation. The current detectors generally have efficiencies well below 10%, while scintillator efficiency is higher than 40% for fast neutrons [27]. A good understanding of photonics and a little nuclear engineering would equip anyone with the knowledge of how scintillators work. An improved understanding of scintillator characteristics, when exposed to different types of radiation, can help vastly improve current detector systems and reduce the risk of nuclear proliferation.

For gamma-induced scintillation, effective atomic number was not the predominant factor in scintillation as one might expect. Temperature, density, and surface area all play a significant role in scintillation light output. One can increase the light yield measured by photo multiplier tubes by focusing light and reducing the temperature for some crystals to get a stronger signal if this is required for a detection scenario. As expected, light yield significantly decreases with distance, but a signal is still generated at long distances beyond the noise level, especially at high energies of incoming radiation. Regardless, gamma-induced scintillation experiments were useful in understanding the basics of scintillator output, and that background helps clarify higher energy experiment results.

Spectroscopy experiments take a considerable amount of time and require a great deal of experimental setup preparation, but the results can be extremely helpful when characterizing specific light output of each crystal. After implementation and calibration of a Photon Counting Spectrometer, the spectral response of the studied scintillators was obtained for different radiation sources like Cobalt-60 and Cesium-137. The most interesting results were from LuAG and LGSO, as the spectra showed dual peak emissions because of their two luminescent centers [29]. More research into this could

produce a better understanding of the probability of occurrence and how it affects the crystal's efficiency. What may be of some value is that the non-doped crystals do not seem to exhibit this dual peak phenomenon, which further corroborates this finding and validates the data from the Photo Counting Spectrometer. Regardless, the purpose of these crystals is to detect fast neutrons for nuclear counter-proliferation activities, and their response to neutrons and how easily one could create such a device is important.

Since the ultimate use of the scintillator would be to detect fast neutrons at a practical distance, a somewhat rudimentary but effective setup was created to analyze scintillator response. The size of the $1ft^3$ box with a $900 femtowatt photoreceiver portable detection device can be reduced significantly to provide a cheap detector with no more than $1,500.00, including crystal and materials. This device could be theoretically the size of one's hand if instrumented correctly. At practical distances all the scintillator signals measured were nowhere near the noise level and distinct enough to move further away from the source. Additionally, at practical distances scintillators can be used effectively in detecting fast neutrons without significant exposure if you have a long enough cable. LGSO seems to be the best candidate for both fast neutrons and gamma detection, while CDWO is the best candidate for gamma detection by several orders of magnitude. Furthermore, as shown in the study of fast neutron response, there seems to be an energy level in which the cross section for inelastic scattering becomes more prevalent than at lower energies. Regardless, each heavy oxide inorganic scintillator produced enough light output to be measured quite easily, effectively, and cheaply, albeit the neutron sources were very powerful.

B.   CHARACTERIZATION IMPROVEMENTS/FUTURE STUDY

The characterization of heavy oxide inorganic scintillators can be improved significantly by the improvement of the PCS and LTCFP setup. The next logical step would be to combine the characteristics of these two creations into a portable setup. Hopefully, this would allow the conduct of spectroscopy and photon counting to further understand the emission response of each crystal when exposed to high-energy neutrons. If this can be done efficiently, it is possible to expand detection to other locations as well.

Additionally, all of the experiments done with gamma radiation need to be repeated with this combined device when exposed to fast neutrons. As an additional consideration, it would be useful to obtain and test BaF_2 and possibly other crystals to understand how they can have a low response to gamma radiation, but a high response to neutrons. This needs to be accomplished to consider development of a detection system that is blind to gamma radiation. More emphasis on engineering a portable apparatus to further test the parameters tested in this thesis would be a valuable contribution to the field and may help the ultimate goal to detect and reduce nuclear proliferation.

THIS PAGE INTENTIONALLY LEFT BLANK

LIST OF REFERENCES

[1]   Department of Defense. (2014, March 4), *Quadrennial defense review* [Online].
        Available:
        http://www.defense.gov/Portals/1/features/defenseReviews/QDR/2014_Quadrenn
        ial_Defense_Review.pdf Accessed Jan. 21, 2016.

[2]   V.D. Ryzhikov et al., "High effective fast neutron detectors based on inorganic
        scintillators," Presented at 2014 IEEE Nuclear Science Symposium & Medical
        Imaging Conference, Seattle, WA, November 2014.

[3]   A.V. Bushuev, *Experimental reactor* Dept. Physics, MIFE (Moscow Institute of
        Physics and Engineering), Moscow, 2008, p. 280.

[4]   S. Glasstone and P. J. Dolan, *The Effects of Nuclear Weapons*, 3rd ed.
        Washington, DC: USDOD and ERDA, 1977.

[5]   R. L. Murray, *Nuclear Energy*. Boston, MA: Butterworth & Heinimann, 2001.

[6]   X.K. Maruyama, Physics of nuclear weapons, unpublished.

[7]   Nuclear fission: Basics. (n.d.). AtomicArchive.com. [Online]. Available:
        http://www.atomicarchive.com/Fission/Fission1.shtml. Accessed Apr. 12, 2016.

[8]   K.S. Krane, *Introductory nuclear physics*, Hoboken, NJ: John Wiley & Sons,
        1988.

[9]   I. Rittersdorf. (n.d.) *Gamma Ray Spectroscopy* [Online]. Available: http://www-
        personal.umich.edu/~ianrit/gammaspec.pdf. Accessed Mar. 13, 2016.

[10]   S. T. Thornton and A. Rex, *Modern physics for scientists and engineers*, Boston,
        MA: Cengage Learning, 2013.

[11]   P. Rodnyi, *Physical processes in Inorganic Scintillators*, Boca Raton, FL: CRC
        Press, 1997, ch. 1, pp. 1–51.

[12]   S. Awadalla, *Solid-state radiation detectors*. Boca Raton, FL: CRC Press Taylor
        & Francis Group, 2015.

[13]   S.O. Kasap, *Optoelectronics and photonics: Principles and practices*, 2nd ed,
        Boston, MA: Pearson, 2013.

[14]   Photomultiplier Tubes. (2007). *Hamamatsu photonic*. [Online]. Available:
        https://www.hamamatsu.com/resources/pdf/etd/PMT_handbook_v3aE.pdf.
        Accessed Jan. 21, 2016.

[15]   G.V. Grinyov et al., *Inorganic scintillators for detector systems*, Berlin, Germany: Springer, 2006.

[16]   P. Lecoq et al., *Inorganic scintillators for detector systems*, Berlin, Germany: Springer, 2006.

[17]   P.R. Rusiecki, "Characterization of heavy oxide inorganic scintillator crystals for direct detection of fast neutrons based on inelastic scattering," M.S. thesis, Dept. Physics, Naval Postgraduate School, Monterey, CA, 2015.

[18]   J.S. Cadiente. "Modeling and investigation of heavy oxide and alkali-halide scintillators for potential use in neutron and gamma detection systems." M.S. thesis, Dept. Physics, Naval Posgraduate School, Monterey, CA, 2015.

[19]   Fig 1. Crystal structure of CdWO 4, wolframite. unit cell is outlined. lone atoms are. (n.d.). Research Gate. [Online]. Available: https://www.researchgate.net/273538432_fig1_Fig-1-Crystal-structure-of-CdWO-4-wolframite-Unit-cell-is-outlined-Lone-atoms-are. Accessed Mar. 10, 2016.

[20]   M.Koshimizu et al., "Scintillation and luminescence properties of a single $CsCaCl_3$ crystal," *Optical Materials,* vol. 36, no. 12, pp. 1930–1933, Oct. 21, 2014.

[21]   *Photomultiplier Tube R943-02*. (n.d.). Hamamatsu photonics. [Online]. Available: https://www.hamamatsu.com/resources/pdf/etd/R943-02_TPMH1115E.pdf Accessed Apr. 2, 2016.

[22]   Hamamatsu Photonics, (n.d.). Instruction manual model C2761 Photomultiplier Cooler. Hamamatsu City, Japan.

[23]   *Stabilized light source for photomuliplier tubes*. (n.d.). Hamamatsu photonics. [Online]. Available: https://www.hamamatsu.com/us/en/L11494.html Accessed Feb. 4, 2016.

[24]   *Visible & IR Femtowatt Photoreceivers*. (2002). New Focus. [Online]. Available: https://assets.newport.com/webDocuments-EN/images/2151_And_2153_User_Manual_RevC.pdf Accessed Apr. 1, 2016.

[25]   *Metal package PMT with cooler photosensor modules H7422 Series*. (n.d.). Hamamatsu. [Online]. Available: https://www.hamamatsu.com/resources/pdf/etd/m-h7422e.pdf Apr. 2, 2016.

[26]   N. Klassen et al., "Correlations between structural and scintillation characteristics of lead and cadmium tunstates," *Nuclear Instruments and Methods in Physics Research Section A: Accelerators, Spectrometers, Detectors and Associated Equipment*, vol. 486, no. 1–2., pp. 431–436, 21 June 2002.

[27] C. Smith, private communication, Jul. and Aug. 2015.

[28] *Gaussian models*. (n.d.). MathWorks. [Online]. Available: http://www.mathworks.com/help/curvefit/gaussian.html?refresh=true. Accessed Apr. 8, 2016.

[29] Y. Kurata et al, "Impact of co-doping on scintillation properties of Lu2xGd2(1-x)SiO5:Ce (LGSO, x=.9)," in *Nuclear Science Symposium Conference Record (NSS/MIC), 2011 IEEE,* Valencia, 2011, pp. 1572-1579

[30] Z.R. Harvey "Neutron flux and energy characterization of a plutonium-beryllium isotopic neutron source by Monte Carlo simulation with verification by neutron activation analysis." Dept. Health Physics and Diagnostic Sciences, University of Nevada, Las Vegas, Las Vegas NV, 2010.

[31] *Polynomial models*. (n.d.). MathWorks. [Online]. Available: http://www.mathworks.com/help/curvefit/polynomial.html. Accessed Apr. 20, 2016.

[32] USNA neutron radiation facilities. (n.d.) Dr Martin E. Nelson [Online]. Available: www.seutest.com/mwiki/images/6/6a/USNA_Radiation_Facilities.pdf. Accessed Feb 5, 2016.

THIS PAGE INTENTIONALLY LEFT BLANK

INITIAL DISTRIBUTION LIST

1. Defense Technical Information Center
    Ft. Belvoir, Virginia

2. Dudley Knox Library
    Naval Postgraduate School
    Monterey, California